Sound generated by flow over two traveling wavy foils in a side-by-side arrangement

Cheng Zhao (赵成); Tao Zhang (张涛) ✉; Yan Yang (杨焱) ✉; ... et. al

Check for updates

CrossMark

View Online

Export Citation

Articles You May Be Interested In

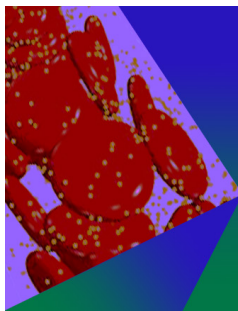Bistable states in the wake of a wavy cylinder

Physics of Fluids (July 2020)

Stretchable wavy metal interconnects

Journal of Vacuum Science & Technology A (July 2004)

Wavy rolls in the Taylor–Bénard problem

Physics of Fluids (January 1998)

Physics of Fluids

Special Topic: Flow and Forensics

Submit Today!

AIP Publishing

Sound generated by flow over two traveling wavy foils in a side-by-side arrangement

View Online   Export Citation   CrossMark

Cheng Zhao (赵成),[1] [iD] Tao Zhang (张涛),[1,a] [iD] Yan Yang (杨焱),[2,a] [iD] and Haibo Dong (董海波)[3] [iD]

AFFILIATIONS

[1]School of Naval Architecture & Ocean Engineering, Huazhong University of Science & Technology, Wuhan, Hubei 430074, China
[2]LHD, Institute of Mechanics, Chinese Academy of Sciences, Beijing 100190, China
[3]Department of Mechanical and Aerospace Engineering, University of Virginia, Charlottesville, Virginia 22904, USA

[a]Authors to whom correspondence should be addressed: zhangt7666@hust.edu.cn and yangyan@imech.ac.cn

ABSTRACT

Numerical simulations are employed to investigate the sound generated by flow over two traveling wavy foils in a side-by-side arrangement by an immersed-boundary-method-based hybrid approach. The effects of Strouhal number (St), phase difference, and lateral spacing (S) between the foils on the flow performance and the sound pressure field are examined. The results imply that the sound produced by a single foil is dominated by the lift dipole, and that the low-amplitude–high-frequency foil can achieve higher thrust and higher sound pressure compared to the high-amplitude–low-frequency foil. For the two side-by-side foils (i.e., an in-phase and anti-phase foil system), the sound pressure fields exhibit distinct features. Specifically, a dipole-like pattern appears during in-phase motion, whereas a monopole-like pattern exists during anti-phase motion. Moreover, the magnitude of the sound pressure increases slightly with increasing S in the in-phase case. However, the sound pressure decreases rapidly when $S < 0.7L$ (foil length) and then remains nearly unchanged when $S > 0.7L$ in the anti-phase case. Furthermore, the anti-phase foil system could improve thrust by increasing power consumption and could generate lower sound pressure compared to the in-phase one due to the distinct differences in wake patterns. The present work is expected to improve the understanding of sound-generation mechanisms of fish-like locomotion and collective motion for relevant biomimetic underwater vehicles.

I. INTRODUCTION

Many aquatic animals, such as fish, dolphins, and tadpoles, utilize their flexible fins or bodies to produce the necessary hydrodynamic forces for swimming. Unsteady flow performance and vortex dynamics have been extensively investigated over recent decades by biologists, physicists, and engineers.[1–3] In addition, significant efforts have been invested into studying high thrust,[4–6] good maneuverability,[7,8] and high efficiency[9–11] with respect to the design of man-made vehicles. However, the near-field sound generation and far-field acoustic propagation of the sounds produced by aquatic and aerial animals have received less attention. The results from investigations into flow-induced noise generated by swimming or flight locomotion can play an important role in biomimetic applications (such as quiet bio-inspired robots). Moreover, studying acoustic signals could help us to understand certain biological functions, such as predation, navigation, communication, and reproduction.[12–15]

Previous studies have used experimental measurements and numerical simulations to investigate the sounds generated by bio-inspired motion. Sueur *et al.*[12] experimentally studied the directional

radiation pattern and the detailed frequency composition of the sound generated by a flying fly. They found that the first harmonic exhibited dipole-like distribution, whereas the second harmonic presented a monopole-like radiation pattern in the horizontal plane of the fly. Bae and Moon[16] performed a numerical simulation of a two-dimensional (2D) bumblebee using a hybrid method. Their results suggested that the transverse motion of the wing generated a primary dipole tone at the frequency of the wing beat due to the torsional angle of the wing motion. Three-dimensional (3D) analyses of flapping wings have also been conducted to investigate the effect of wing kinematics on sound generation.[14,17–20] Geng *et al.*[17] reported that the deformation of a flexible wing could help lower the sound pressure in all directions. Wang and Tian[20] systematically examined the effects of several parameters (including wing shape and flexibility) on the acoustic field based on a fluid–structure–acoustics interaction direct numerical simulation (DNS) solver. Their results indicated that the wing shape did not affect directivity, while appropriate flexibility could reduce the acoustic output. In another recent study, Seo *et al.*[14] demonstrated that mosquitoes could adopt a high wing aspect ratio, high beat frequency, and small

stroke amplitude to generate high-intensity wing tones for acoustic communication.

Although some studies have investigated flapping wings or relevant appendages, research on undulatory swimming remains limited. Khalid et al.[21] quantitatively investigated the flow noise produced by an oscillating hydrofoil for various kinematics and flow parameters. They reported that the distribution of sound pressure levels at the oscillating frequency exhibited dipole-like patterns and the magnitudes depended on the Reynolds number and Strouhal number. A recent study[22] on the acoustic emission of undulatory swimmers revealed that a vertically oriented dipole dominated the transient acoustic response in the near and far fields for both anguilliform and carangiform swimming gaits. It should be noted that the Ffowcs Williams–Hawkings (FW–H) method[21] and the inviscid assumption[22] were used in previous simulations; hence, the previously mentioned studies mainly focused on sound radiation. Accordingly, there is a lack of further understanding with regard to the generation and propagation mechanisms of sound during undulatory propulsion. Moreover, unanswered questions remain regarding the sound generated by flow over multiple foils. Previous studies[23–25] have indicated that the flow interference of foils would affect the flow patterns and propulsive performance. However, the sound pressure fields generated by the two foils associated with fish schools have not been examined. All the previously mentioned points motivated the present study.

In this work, the sound generated by two traveling wavy foils in a side-by-side arrangement is numerically investigated using a hybrid computational acoustics method. The flow field is simulated using a high-fidelity immersed-boundary-method-based DNS solver, and the acoustic field is predicted by solving the acoustic perturbation equations (APEs). In addition, the effects of phase difference and lateral spacing between the two foils on flow performance and sound generation are examined. The remainder of this paper proceeds as follows. In Sec. II, the problem definition, numerical method, case setup, and validations are described. The simulation results for the single foil and two foils are analyzed in Sec. III, and Sec. IV presents the conclusions.

II. PHYSICAL PROBLEM AND NUMERICAL METHODOLOGY

A. Problem definition

In this study, the geometry of the 2D foil at an equilibrium state is modeled by the cross-section of the NACA 0012 airfoil. The chord length is L, and the traveling wave kinematics are imposed on the foil to mimic undulatory swimming. Based on Gilmanov's approach,[26] the foil's lateral displacement is described as follows:

$$y(x, t) = a(x)\sin(kx - 2\pi f_0 t + \varphi), \quad x \in [0, 1]. \quad (1)$$

Here, $y(x, t)$ is the instantaneous transverse position (which is non-dimensionalized by the foil length L), k is the wave number (which is set to 2π), f_0 is the undulatory frequency, φ is the initial phase angle, and $a(x)$ describes the amplitude envelope of the traveling wave. Assuming that $a(x)$ varies non-linearly along the foil length, the wave amplitude is described as a quadratic function of x,

$$a(x) = a_0 + a_1 x + a_2 x^2. \quad (2)$$

This quadratic function was fitted through the experimental curve[27] and is widely used as the kinematic model for undulatory swimming.[10,22,26,28–31]

Two dimensionless parameters [the Reynolds number (Re) and Strouhal number (St)] are used to define the flow conditions and kinematics of the foil, which can be expressed as follows:

$$Re = \frac{U_0 L}{\nu_0}, \quad St = \frac{2a_{\max} f_0}{U_0}, \quad (3)$$

where U_0 is the velocity of the incoming flow, ν_0 is the kinematic viscosity of the fluid, and $2a_{\max}$ is the peak-to-peak tail beat amplitude.

In this study, a 2D foil model is considered to improve computational efficiency without loss of representativeness for current object. Previous studies[30,32] have indicated that most of the 2D simulation results for an undulating tadpole closely matched the 3D results, with the exception of propulsive efficiency at $Re = 7200$. Moreover, Hemelrijk et al.[33] revealed that the 2D results for a mullet at $Re \sim 1.2 \times 10^3$ were similar to the 3D experimental data at $Re \sim 20 \times 10^3$. Consequently, the 2D model at $Re = 1000$ was selected herein to reduce difference between the 2D and 3D models. For the acoustic simulation, the inflow Mach number (Ma) is expressed as the ratio of U_0 to the speed of sound c_0, $U_0/c_0 = 0.01$. Two typical undulating parameters with different amplitudes and frequencies are considered. The first is termed a low-amplitude–high-frequency (LA–HF) foil, and its constants were selected as $a_0 = 0.02$, $a_1 = -0.08$, and $a_2 = 0.16$. The second is termed a high-amplitude–low-frequency (HA–LF) foil, with $a_0 = 0.04$, $a_1 = -0.16$, and $a_2 = 0.32$. This means that the HA–LF foil has twice the amplitude and half the frequency of the LA–HF foil. The $a_{\max}$ value is 0.1 for the LA–HF foil and 0.2 for the HA–LF foil, while St varies from 0.3 to 0.6 at intervals of 0.05 by changing f_0. Figure 1 presents a sequence of midlines for the foil during a tail-beat period with 12 time intervals.

Figure 2 presents a schematic diagram of the side-by-side foil system. The present study considers two typical cases: an in-phase foil
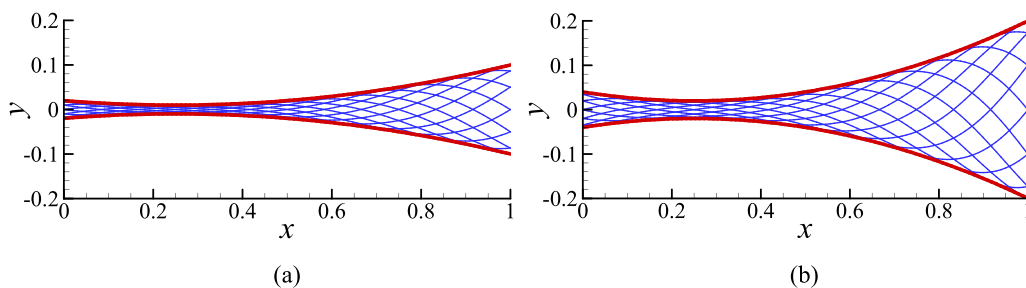

FIG. 1. The midlines of the LA–HF (a) and HA–LF (b) foils during a tail-beat period with 12 time intervals (red line represents the amplitude of the traveling wave).
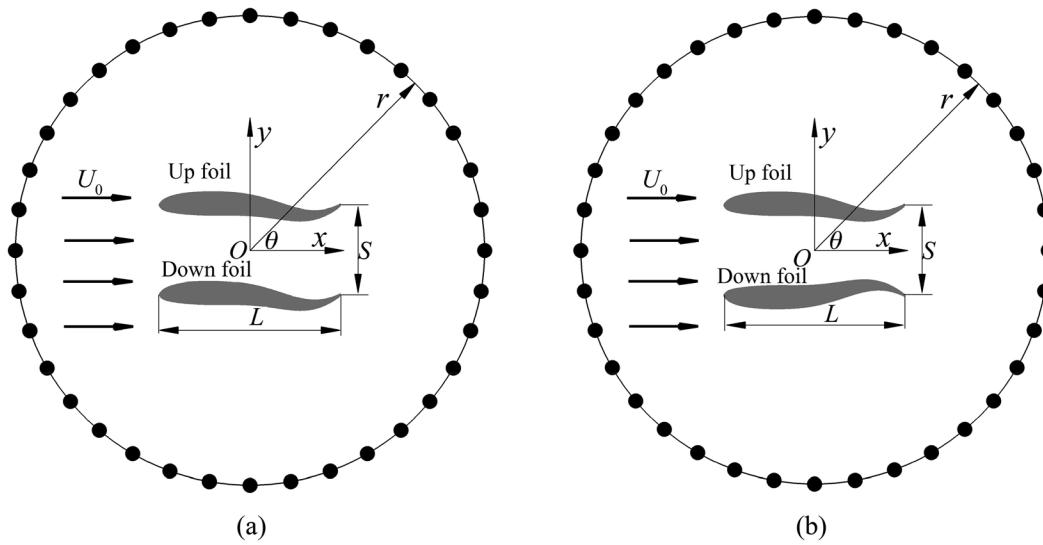
FIG. 2. Schematic diagram of the in-phase (a) and anti-phase (b) foil systems.

system ($\varphi_{up} - \varphi_{down} = 0$) and an anti-phase foil system ($\varphi_{up} - \varphi_{down} = \pi$). The initial distance between the tails of the foils is defined as the lateral spacing S. The origin coordinate O is placed at the midpoint of the two foils, and the coordinates parallel and normal to the free stream are denoted as x and y, respectively. Furthermore, the polar coordinate system (r, θ) with pole O and polar axis x is defined for the acoustic discussions.

B. Numerical method

A hybrid computational acoustic method is implemented to simulate the flow-induced sound. The flow field is simulated by solving incompressible Navier–Stokes (INS) equations that can be written in the following vector form:

$$\nabla \cdot \boldsymbol{U} = 0, \qquad (4)$$

$$\frac{\partial \boldsymbol{U}}{\partial t} + (\boldsymbol{U} \cdot \nabla)\boldsymbol{U} = -\frac{1}{\rho_0}\nabla P + \nu_0 \nabla^2 \boldsymbol{U}, \qquad (5)$$

where ρ_0, ν_0, $\boldsymbol{U}$, and P are the incompressible flow density, kinematic viscosity, velocity vector, and pressure, respectively.

An in-house designed finite-difference-based Cartesian grid immersed boundary method is employed to solve Eqs. (4) and (5). The INS equations are non-dimensionalized by the foil length, L, incoming flow velocity, U_0, and density, ρ_0. The INS equations are spatially discretized with a second-order central difference scheme using a cell-centered, collocated (non-staggered) arrangement of the primitive variables (U_i, P). The equations are integrated in time using the fractional step method, which consists of three sub-steps. In the first sub-step, a modified momentum equation is solved, and an intermediate velocity is obtained. Specifically, a second-order Adams–Bashforth scheme is applied to the convection terms, and a Crank–Nicolson scheme is used for the diffusion terms. The second sub-step involves solving the pressure correction Poisson equation. Finally, the pressure and velocity are updated when the pressure

correction is obtained. The complex flow around a moving boundary is resolved using a ghost-cell-based sharp-interface-immersed boundary method. This solver has been successfully applied previously to simulate bio-inspired flow problems with complex geometries and moving boundaries.[34–38]

The sound pressure field is simulated by solving the acoustic perturbation equations (APEs).[39] The APEs with incompressible acoustic sources are written as follows:

$$\frac{\partial p'}{\partial t} + \bar{c}_0{}^2 \nabla \cdot \left(\bar{\rho}_0 \boldsymbol{u}' + \bar{U} \frac{p'}{c_0{}^2} \right) = 0, \qquad (6)$$

$$\frac{\partial \boldsymbol{u}'}{\partial t} + \nabla(\bar{U} \cdot \boldsymbol{u}') + \nabla\left(\frac{p'}{\bar{\rho}_0} \right) = \frac{\nabla P'}{\rho_0}. \qquad (7)$$

Here, p' and $\boldsymbol{u}'$ represent the sound pressure and perturbation velocity vector, respectively, c_0 is the speed of sound, and the bar symbol denotes time-averaged quantities, which are the average values during several periods after achieving a steady-state. The left-hand sides of the APEs describe the sound pressure propagation in a non-uniform mean flow field, and the right-hand-side terms are the acoustic sources. The acoustic sources of the x and y components are expressed as $(\partial P'/\partial x)/\rho_0$ and $(\partial P'/\partial y)/\rho_0$, respectively. Here, $P' = P - \overline{P}$ is the incompressible perturbation pressure.

The APEs are non-dimensionalized by the foil length, L, speed of sound, c_0, and density, ρ_0. The sound pressure is non-dimensionalized with $\rho_0 c_0{}^2$. The APEs are spatially discretized with a dispersion relation preserving (DRP) scheme[40] and integrated in time using a low-dissipation and low-dispersion Runge–Kutta (LDDRK) scheme.[41] A tenth-order spatial filtering[42] is applied to eliminate grid-to-grid oscillations. At the computational domain boundaries, the radiation boundary conditions[43] are applied to absorb the outgoing sound waves. The sharp-interface-immersed-boundary-method based acoustic solver implemented in our previous work[44,45] is further developed to resolve the moving boundary.

C. Case setup

To measure the flow performance and acoustic characteristics of the foil, the drag coefficient, thrust coefficient, lift (i.e., lateral force) coefficient, power coefficient, and effective sound pressure (denote as C_D, C_T, C_L, C_{PW}, and p'_{RMS}) are defined as follows:

$$C_D = -C_T = \frac{F_D}{0.5\rho_0 U_0^2 L}, \quad C_L = \frac{F_L}{0.5\rho_0 U_0^2 L},$$

$$C_{PW} = \frac{P_f}{0.5\rho_0 U_0^3 L^2}, \quad p'_{RMS} = \sqrt{\frac{1}{t}\int_0^t p'^2 dt}. \tag{8}$$

Here, F_D and F_L are the drag and lift acting on the foil, respectively, P_f is the hydrodynamic power of the foil, and p' is normalized by $\rho_0 c_0^2$.

The computational grid and flow boundary conditions are presented in Fig. 3. For the flow solver, a constant velocity is specified at the upstream boundary and lateral boundaries, while a zero-gradient velocity condition is applied at the downstream boundary. A homogeneous Neumann boundary condition is used for the flow pressure at all boundaries. For the acoustic solver, radiation boundary conditions are applied at all domain boundaries. For the computational grid, the APEs are solved on the same Cartesian grid as the flow solver. High-resolution grids are generated in the vicinity of the foil and in the wake to resolve the boundary layer and vortex structure of the flow field more effectively. Since flow simulations require a much finer grid than acoustic simulations near the foil, grid independence tests are performed based on the drag and lift histories. The minimum grid spacings of the coarse, medium, and fine grids are $0.01L$, $0.005L$, and $0.0035L$, respectively. The grid spacing is stretched to $1.9L$, and the uniform grid is applied from the local position to the domain boundary to resolve the far-field sound pressure waves. The computational domain size of uniform grid near the foil is $1.5L \times 1.5L$, and the total computational domain size is $200L \times 200L$. The total numbers of grid nodes for the coarse, medium, and fine grids are 660×468

($\approx 0.309 \times 10^6$), 960×768 ($\approx 0.737 \times 10^6$), and 1280×1024 ($\approx 1.311 \times 10^6$), respectively.

The instantaneous drag coefficients and lift coefficients for a single foil with three different grid spacings are presented in Fig. 4. It shows that the maximum differences of the peak value for drag coefficient and lift coefficient between the medium grid case and the fine grid case are less than 2% and 1%, respectively. These results demonstrate that the simulation results were grid-independent.

D. Validations

Although the present method was verified by benchmark acoustic scattering and flow-induced noise problems in our previous studies,[44–46] two cases are performed and compared with the literature results to validate the accuracy of the flow solver for fish-like swimming and the hybrid computational acoustic method for moving bodies.

The flow over a traveling wavy foil at $Re = 5000$ is first computed, and the kinematics of the foil are described by Eq. (1), with $f_0 = 2$ and $\varphi = \pi/2$. The time histories of the drag and lateral force coefficients during one cycle are presented in Fig. 5. The coefficient of the determination (R^2) value is used to evaluate the error between the present results and the reference results. The R^2 values of the drag and lateral force coefficients are 0.875 and 0.997, respectively. The current results match the numerical solutions obtained by Dong and Lu,[10] which validates the accuracy of the flow solver for fish-like swimming.

The sound generated by flow past an oscillating cylinder is further simulated to validate the effectiveness and accuracy of the acoustic solver. Here, the Reynolds number based on incoming velocity, U_0, and the diameter of cylinder, D, is 150, and the Mach number is 0.2. The motion equation is prescribed as $y(t) = 0.2\sin(2\pi t \times 0.15)$, and the schematic diagram is depicted in Fig. 6(a). The directivity at $r = 80D$ is presented in Fig. 6(b), and the current result is in good agreement with the DNS solution obtained by Hattori and Komatsu.[47]
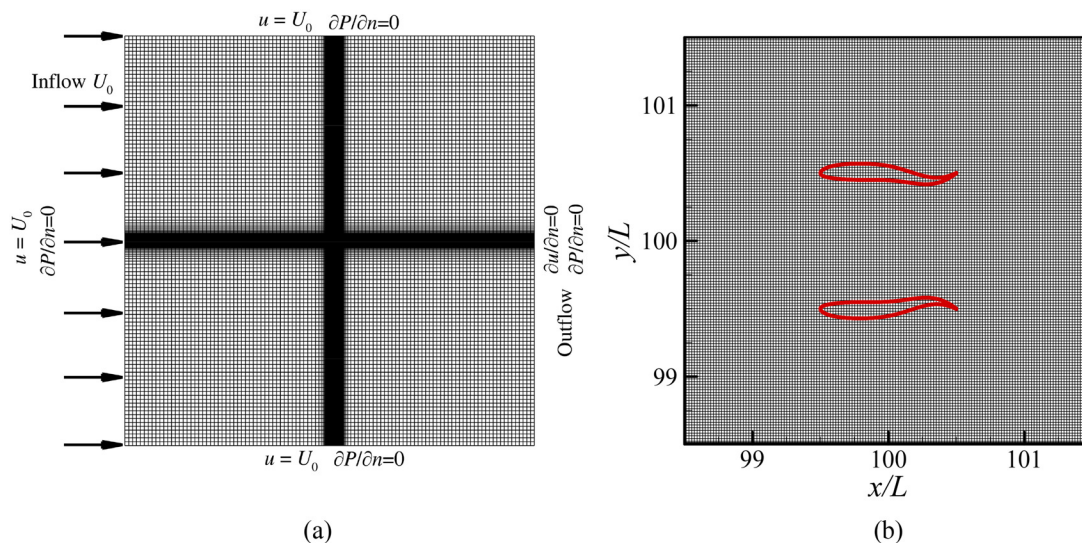

FIG. 3. (a) Schematic diagram of the medium computational grid and flow boundary conditions. (b) Computational grid of medium size ($0.005L$) around the foil (only every fourth grid is plotted).
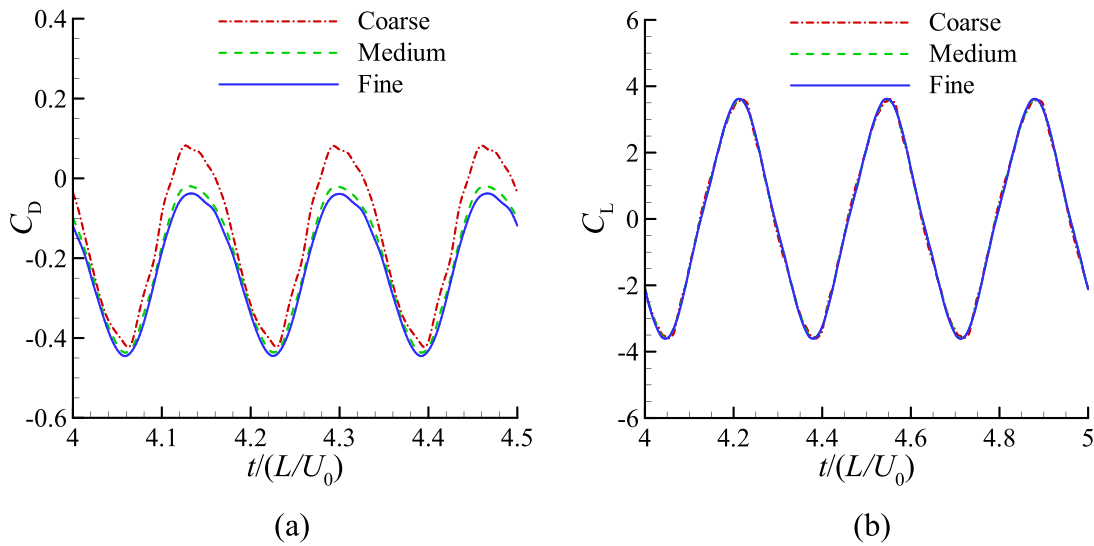
(a)　　　　　　　　　　　　　　　(b)

FIG. 4. Comparison of the drag coefficients (a) and lift coefficients (b) of the single foil for grid independence study.

To conclude, these two cases demonstrate the accuracy and feasibility of the hybrid computational method for flow-induced sound problems with moving boundaries.

III. RESULTS AND DISCUSSION

In this section, the flow performance and the sound pressure field of a single foil are first considered. Based on this, sound generation by two foils in a side-by-side arrangement is further investigated. The flow simulation is carried out for 20 oscillation cycles, and the last ten cycles are applied for the acoustic simulation after achieving a steady-state. Within each flow time step, the acoustic field is solved for 200 time steps. Moreover, 36 monitor points (shown in Fig. 2) at a distance of $r = 60L$ are used to record the far-field sound signals. At this distance, the acoustic field is a sufficient distance from the foil to avoid

recording the pseudo-sound wave generated in the near-field due to the transitional wake. In the post-processing results, the sound pressure is non-dimensionalized by $\rho_0 c_0^2$, the acoustic source is non-dimensionalized by U_0^2/L, and the vorticity field is non-dimensionalized by U_0/L (unless stated otherwise).

A. Single traveling wavy foil

The time-averaged drag coefficients and the RMS values of the lift coefficients against St for the LA–HF foil ($a_{max} = 0.1$) and the HA–LF foil ($a_{max} = 0.2$) are presented in Figs. 7(a) and 7(b). It is evident that both drag coefficients decrease with increasing St. When St of the LA–HF foil is greater than 0.42, negative drag is generated, which means that it acts as a thrust force on the foil. However, the threshold for the St of thrust generation for the HA–LF foil is about 0.57. The results indicate that the drag (thrust) coefficient of the LA–HF foil is lower (higher) than that of the HA–LF one. Moreover, both lift coefficients of the two foils increase monotonically with increasing St. The lift coefficient of the LA–HF foil is higher than that of the HA–LF foil. For example, the RMS values of the lift coefficient at $St = 0.6$ are approximately 2.5 and 1.0 for the LA–HF and HA–LF foils, respectively. The current results indicate that when St is constant, the LA–HF foil can achieve a higher thrust or a lower drag production and a larger lift compared with the HA–LF foil. The time-averaged power coefficients C_{PW}^{ave} against St for the LA–HF and HA–LF foils are presented in Fig. 7(c). Both power consumptions of the two foils increase with increasing St. The power consumption of the HA–LF foil is slightly higher than the LA–HF foil when $St < 0.35$. However, the power consumption of the LA–HF foil increases much more rapidly and is higher than that of the HA–LF foil when $St > 0.35$, due to the more rapid increase in thrust and lift coefficients.

The instantaneous z-vorticity (ω_z) contours at the time of maximum tail displacement of the LA–HF and HA–LF foils for $St = 0.60$ are presented in Figs. 8(a) and 8(b). Periodic vortices behind the foil form a reverse von Kármán street, and thrust is generated under this
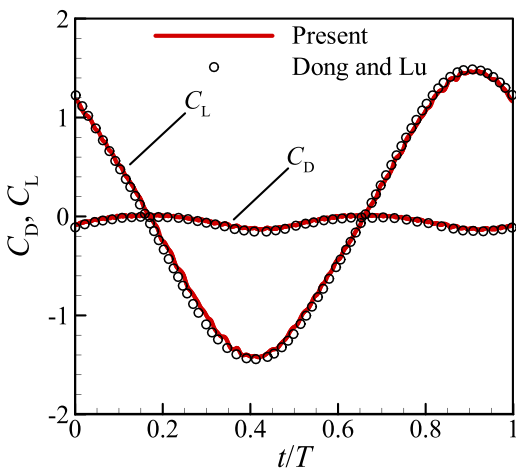

FIG. 5. Comparison of force coefficients during one cycle for the single foil. Line: this study; symbol: Dong and Lu.[10]
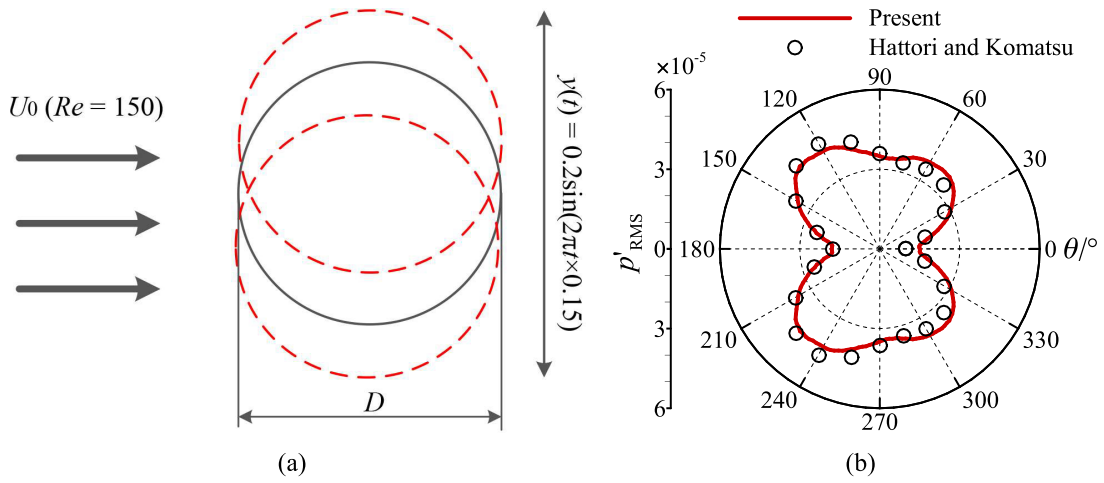
FIG. 6. Schematic diagram of flow past an oscillating cylinder (a) and directivity at $r = 80D$ (b).
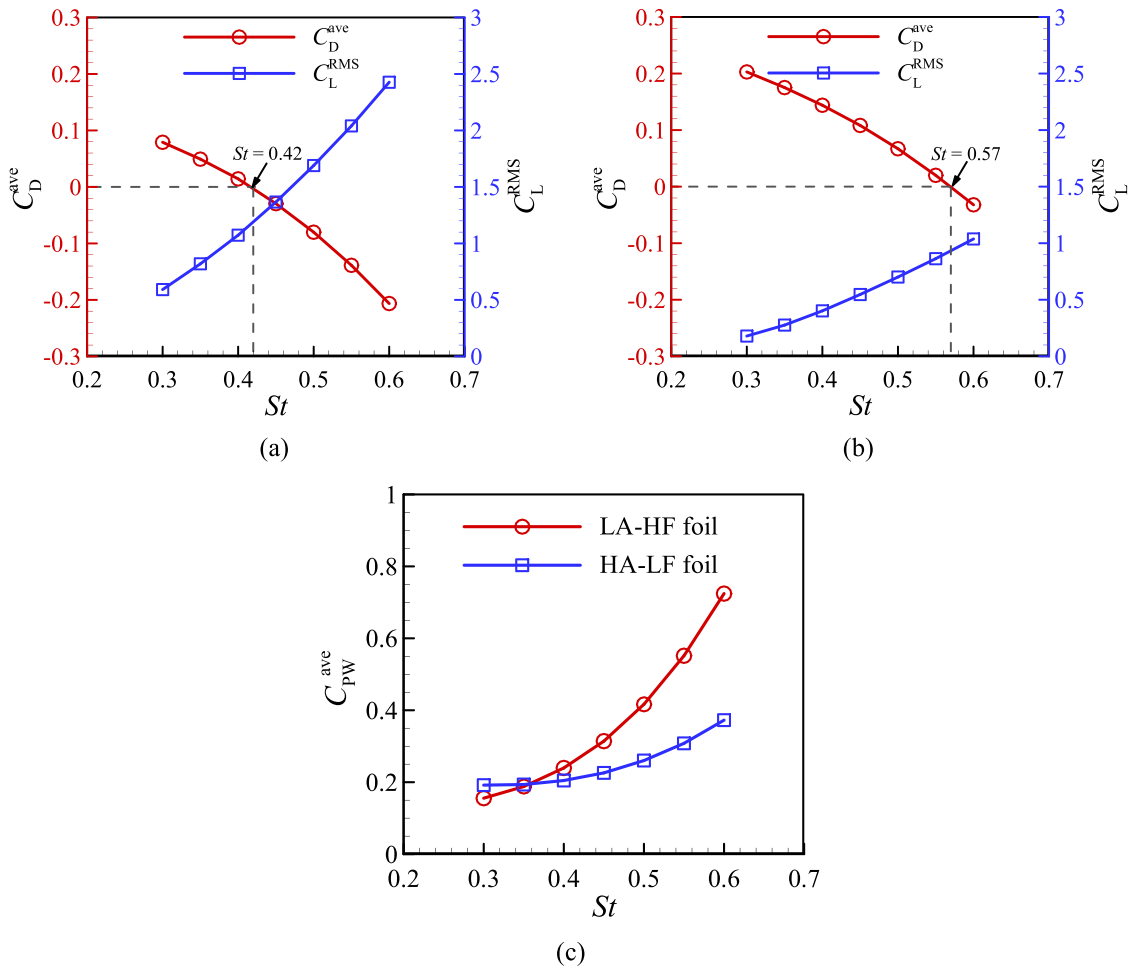

FIG. 7. The time-averaged drag coefficients and the RMS values of the lift coefficient against St for the LA–HF (a) and HA–LF (b) foils. (c) The time-averaged power coefficient against St for the LA–HF and HA–LF foils.
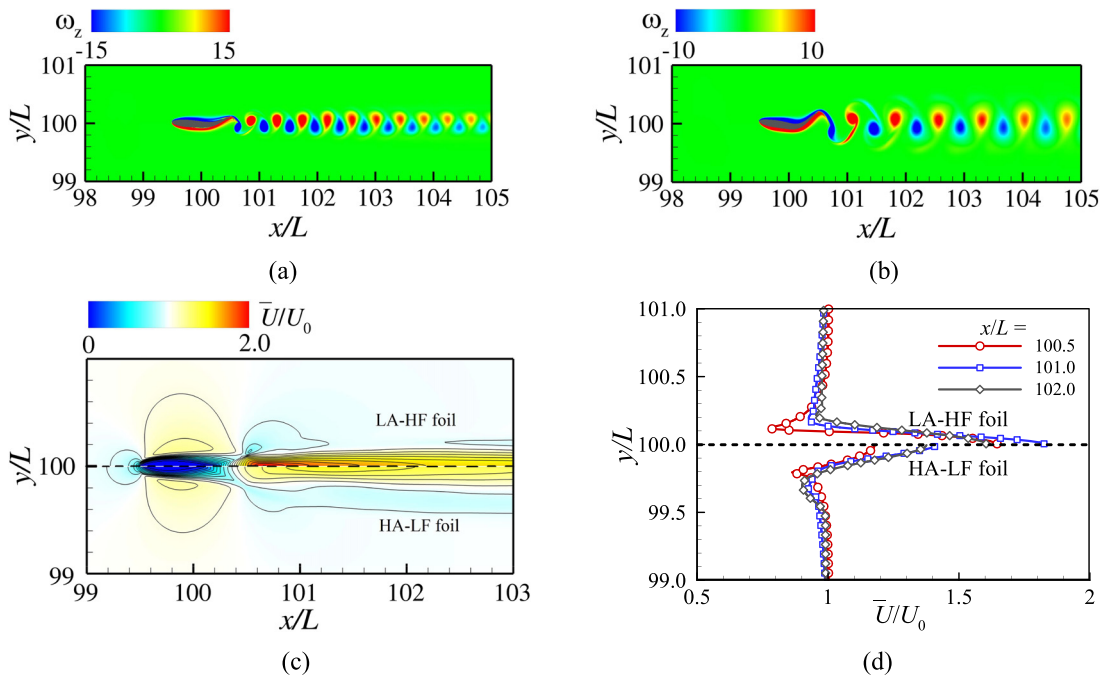
FIG. 8. Instantaneous z-vorticity contours of the LA–HF (a) and HA–LF (b) foils. Time-averaged streamwise velocity contour (c) and streamwise velocity profiles (d) at $St = 0.6$, upper and lower halves of each figure correspond to the LA–HF and HA–LF foils.

condition. As St is constant, the LA–HF foil is twice the oscillation frequency of the HA–LF foil; thus, the vortex shedding frequency of the latter is approximately half that of the former. The time-averaged streamwise velocity and streamwise velocity profiles are presented in Figs. 8(c) and 8(d), respectively. The upper and lower halves of each figure correspond to the LA–HF and HA–LF foils, respectively. The LA–HF foil produces a stronger momentum jet at the centerline of the

wake and generates higher thrust due to the formation of a stronger reverse von Kármán vortex street.

The sound pressure fields generated by two foils corresponding to Fig. 8 are presented in Fig. 9, where it is evident that both sound pressure fields of the foils exhibit a dipole-like pattern. Although the St of the LA–HF foil is equal to that of the HA–LF foil, different sound pressure fields can be clearly observed due to the difference in
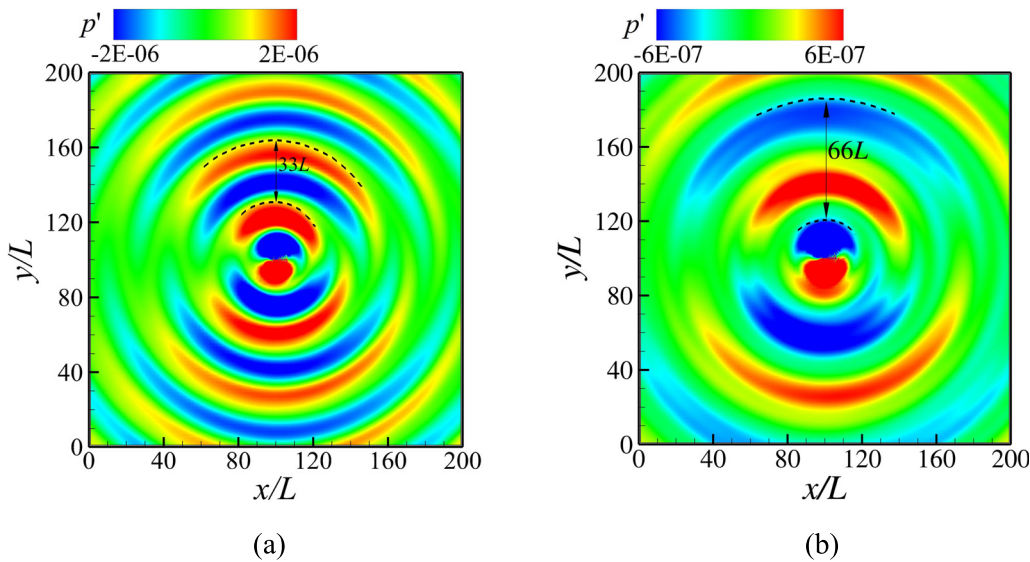

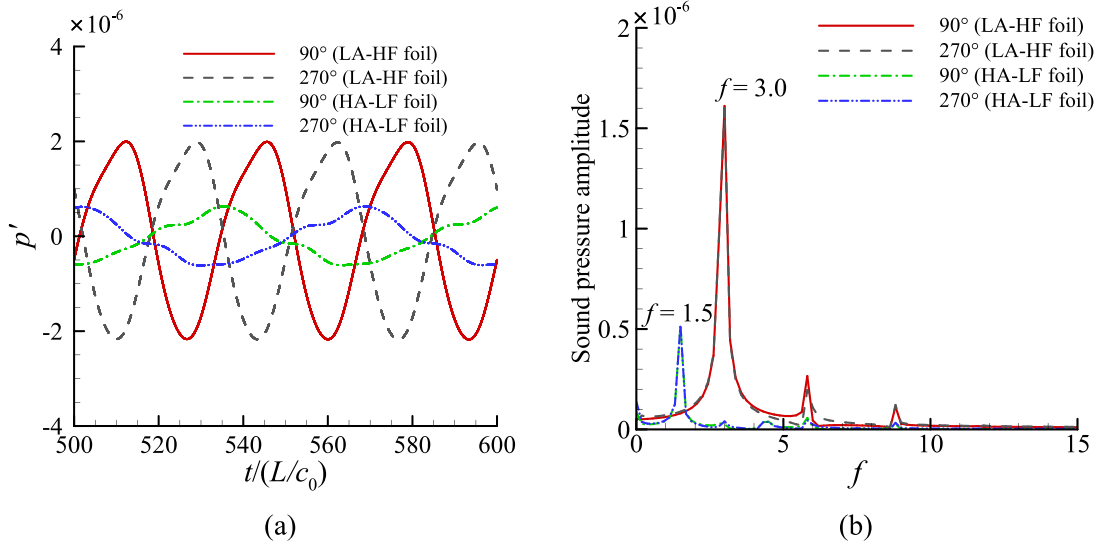**FIG. 9.** Instantaneous sound pressure fields of the LA–HF (a) and HA–LF (b) foils at $St = 0.6$.

FIG. 10. (a) Time histories of the sound pressure in the vertical direction of the LA–HF and HA–LF foils for $St = 0.6$. (b) Frequency spectrum of the sound pressure.

undulatory frequency. As shown in Fig. 9, the wavelengths (vertical distances between the two dotted lines) of the LA–HF and HA–LF foils are approximately $33L$ and $66L$, respectively. Both wavelengths are close to the theoretically predicted values ($33.3L$ and $66.6L$) based on the undulatory frequency and inflow Mach number, which can be expressed as $c_0 L/(Ma \cdot f_0)$. The sound pressure waves are generated in response to vortex shedding, which is dominated by the oscillation frequency. It should be noted that the Mach number is low in the present study; hence, the Doppler effect has a very small influence on sound propagation.

As the sound pressure field of the single foil presents a vertically oriented dipole directivity, the time histories of sound pressure measured at $r = 60L$ and $\theta = 90°$ and $270°$ of the two foils for $St = 0.6$ are

recorded in Fig. 10(a). The figure demonstrates that the amplitude of sound pressure for the LA–HF foil is larger than that of the HA–LF foil. To elucidate the frequency spectrum of the sound pressure, fast Fourier transform (FFT) was conducted to extract the frequency components and their contributions, as shown in Fig. 10(b). It is found that the first harmonic of the LA–HF foil is approximately twice that of the HA–LF foil, and both fundamental frequencies are equal to their respective undulatory frequency. It should be mentioned that the frequency f_0 is also the strongest in the constitution of the lift force. This phenomenon is similar to that of sound generated by flow past a stationary circular cylinder.[48]

The directivities measured at $r = 60L$ against St for the LA–HF (dashed line) and HA–LF (solid line) foils are presented in Fig. 11(a).
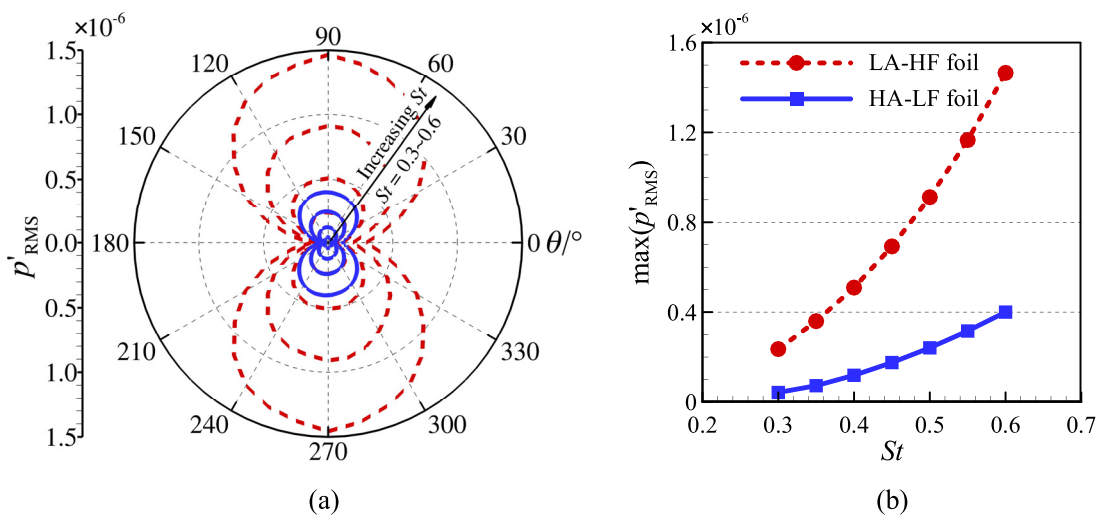

FIG. 11. (a) Directivities of the single foil at varied St (dashed line: LA–HF foil, solid line: HA–LF foil). (b) Maximum effective sound pressure against St.

The directivities of the single foil at different kinematics retain the dipolar nature of the sound pressure field. Moreover, the amplitudes of the sound pressure in all directions increase monotonically with increasing St. A similar result was reported in a previous study of unsteady potential/inviscid flow solutions.[22] The maximum effective sound pressure against St is presented in Fig. 11(b), where it can be observed that the magnitude of the sound pressure of the LA–HF foil is higher than that of the HA–LF foil. These results indicate that when St is constant, the foil can improve the thrust by increasing the undulatory frequency, although the sound pressure also increases due to high lift fluctuations. Moreover, the increasing rate of p'_{RMS} of the LA–HF foil is much higher than that of the HA–LF foil, which is similar to the results of the hydrodynamic forces and the power consumption.

B. Two in-phase traveling wavy foils

In this section, the sound generated by two in-phase traveling wavy foils in a uniform flow is simulated to explore the acoustic characteristics. In addition, the effect of initial lateral spacing S on the hydrodynamics and sound pressure field is analyzed. The kinematics of each foil in the in-phase foil system are set as $a_{max} = 0.1$ (LA–HF foil) and $St = 0.45$, and five different lateral spacings are considered (0.3L, 0.5L, 0.7L, 1.0L, and 1.5L). The reason for choosing current kinematics is that the thrust-generation is just satisfied for the single LA–HF foil.

The instantaneous z-vorticity contours of the in-phase system at $S = 0.3L$ and 1.5L are presented in Fig. 12. When the lateral spacing is large, vortices with the same sense of rotation are shed from the two foils independently. However, the two vortices merge into a new vortex at a small lateral spacing, and the flow field is similar to the period vortex street shed from the single foil. The instantaneous acoustic source distributions of the x and y components corresponding to Fig. 12 are shown in Figs. 13(a) and 13(b), respectively. It is found that the acoustic sources present similar distributions to the vorticity field. The dominant acoustic sources originate mainly at the trailing and leading edges, which can be attributed to the flow separation and vortex shedding. The instantaneous sound pressure fields of the in-phase system at $S = 0.3L$ and $S = 1.5L$ are presented in Figs. 13(c) and 13(d), respectively, where it is found that the sound pressure fields of the in-phase foils are very similar to the single foil (which presents a dipolar nature), and the lift dipole dominates the sound. This implies that the sound pressure waves are generated primarily by periodic vortex shedding. For the two in-phase foils, two vortices are shed simultaneously

from the same sides. Moreover, negative pressure is generated on the same vortex-shedding sides of two foils, whereas positive pressure is generated on the other side, and both waves propagate upward and downward. As the geometry of the foil is very small compared to the length of the sound wave $[= c_0 L/(Ma \cdot f_0) = 44.4L]$, the reflection of the sound wave from the foil can be neglected. In this way, the sound pressure generated by the foil system presents the superposition of two acoustic dipoles with the same amplitude and phase generated by the foils.

Figure 14(a) presents the time histories of the drag and lift coefficients of the up and down foils at $S = 0.3L$. The results indicate that the lift coefficients of the up and down foils are in phase, and the drag coefficients are in anti-phase of 180° phase difference at small lateral spacings. The frequency of the drag coefficient is equal to that of the lift coefficient. The time-averaged drag coefficient, C_D^{ave}, the time-averaged lift coefficient, C_L^{ave}, the amplitude of the drag coefficient fluctuation, $(C_D)_{amp} = ABS\,(C_D - C_D^{ave})$, where ABS is the absolute value, and the amplitude of the lift coefficient fluctuation, $(C_L)_{amp} = ABS\,(C_L - C_L^{ave})$ of the down foil at different lateral spacings are shown in Fig. 14(b). It is evident that the drag and lift coefficients gradually approach the value of the single foil with increased lateral spacing, and the flow interference between the foils is weak when $S > 1.5L$. However, the time-averaged net force coefficient in the streamwise direction is positive at small lateral spacings, which means that it acts as a drag force. This can be attributed to the lateral interference between the foils and the formation of the von Kármán street, as shown in Fig. 12(a). Moreover, results reveal that $(C_D)_{amp}$ and $(C_L)_{amp}$ present opposite features, $(C_D)_{amp}$ decreases with increasing lateral spacing, while $(C_L)_{amp}$ increases slightly.

The directivities measured at a distance of $r = 60L$ at varied lateral spacings are shown in Fig. 15(a). The single foil ($S = 0.0L$) is also plotted for comparison. All the radiation patterns of the in-phase foil system with different lateral spacings retain the lift-dipolar form. The amplitude of the sound pressure increases slightly with increasing lateral spacing, which can be attributed to the increase in $(C_L)_{amp}$, as shown in Fig. 14(b). In addition, the amplitudes of the sound pressure are approximately twice that of the single foil (circle line in the figure). This is consistent with our previous analysis in Fig. 13 that the sound pressure is a linear superposition of two uniform dipole sources with small position staggering. As the sound pressure is high in the vertical direction ($\theta = \pm 90°$), the frequency spectrum of the sound pressure for varied lateral spacings at $(60L, 90°)$ monitor point is presented in Fig. 15(b). Similar frequency spectrum distributions can be observed

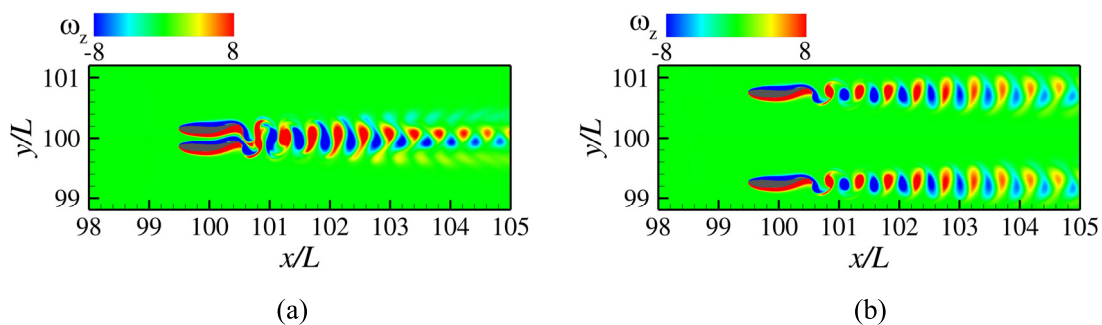FIG. 12. Instantaneous z-vorticity contours of the in-phase foil system at $S = 0.3L$ (a) and $S = 1.5L$ (b).
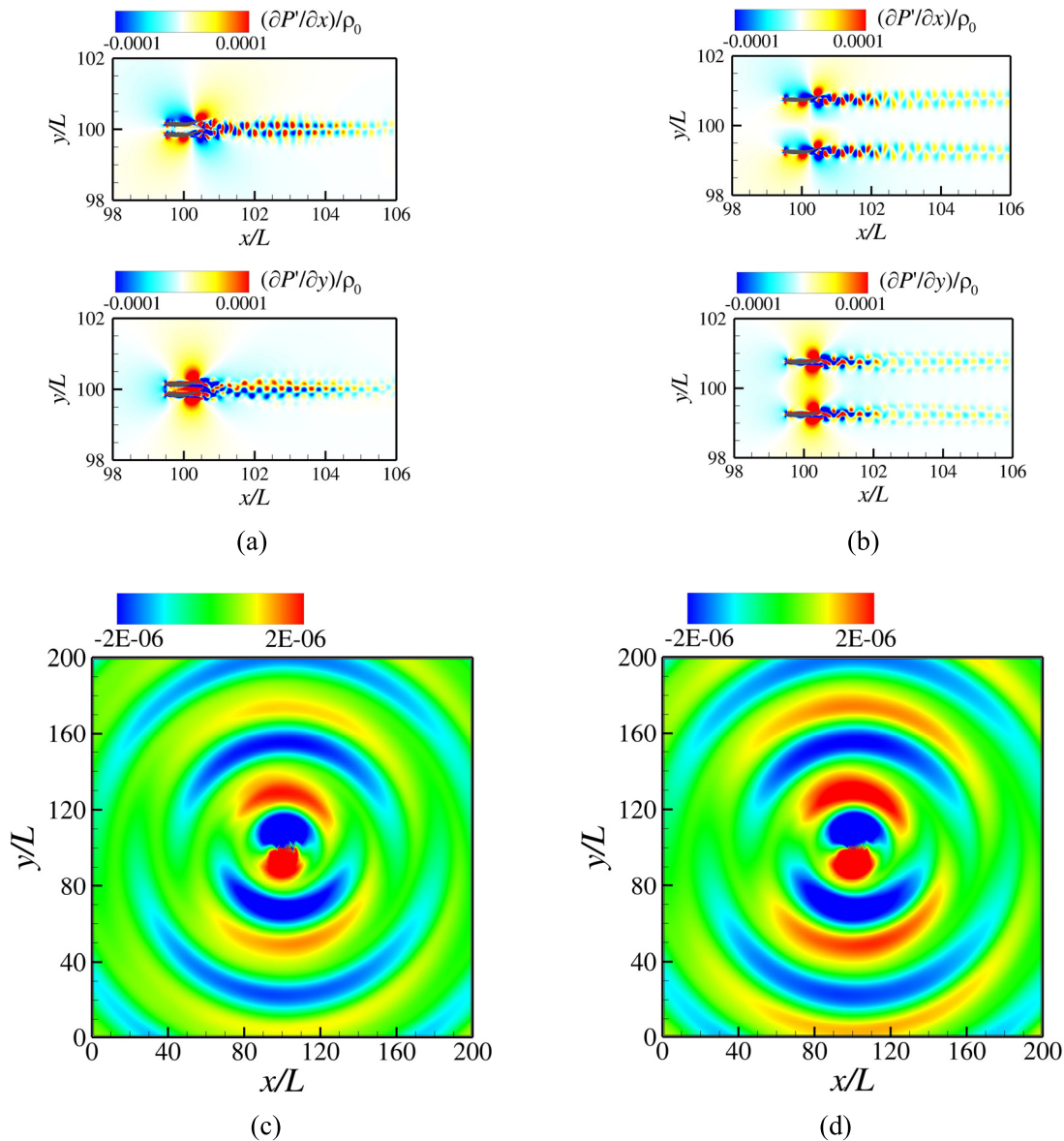
FIG. 13. Instantaneous acoustic source distributions of the in-phase foil system at $S = 0.3L$ (a) and $S = 1.5L$ (b). Instantaneous sound pressure fields of the in-phase foil system at $S = 0.3L$ (c) and $S = 1.5L$ (d).

for the in-phase system at all lateral spacings, and the sound pressure field is dominated by the oscillation frequency, which is similar to that of the single foil.

C. Two anti-phase traveling wavy foils

In this section, the flow performance and sound pressure field generated by the anti-phase foil system are analyzed to explore the acoustic characteristics and to compare them with the in-phase results. The parameters are set to the same as the in-phase cases, where St is set as 0.45. Figure 16(a) shows the time histories of the drag and lift coefficients at $S = 0.3L$, where it can be observed that the

lift coefficients of the up and down foils are in anti-phase, whereas the drag coefficients are in-phase, which is different from the in-phase foil system. When the up foil takes the maximum lift, the down foil takes the minimum value, and the reverse is also true. Moreover, the frequency of the drag coefficient is equal to the lift, which is similar to the in-phase case. The time-averaged lift coefficients of the up and down foils are not zero due to the flow interference between the two foils.

The time-averaged drag coefficient, time-averaged lift coefficient, amplitude of the drag coefficient fluctuation $(C_D)_{amp}$, and amplitude of the lift coefficient fluctuation $(C_L)_{amp}$ of the down foil at different
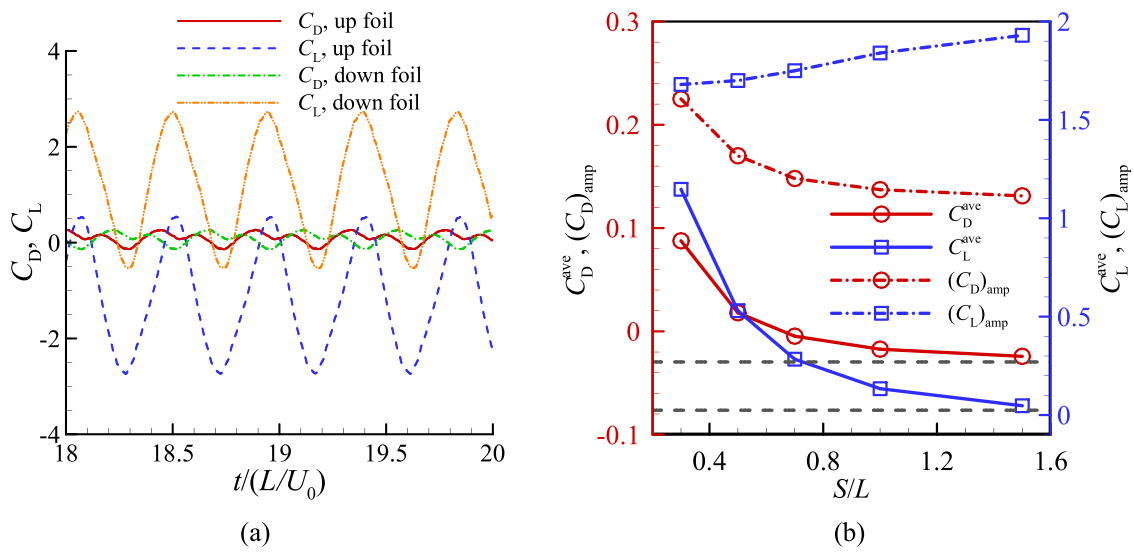
FIG. 14. (a) Time histories of the drag and lift coefficients of the in-phase foil system at $S = 0.3L$. (b) Time-averaged drag coefficient, time-averaged lift coefficient, amplitude of the drag coefficient fluctuation $(C_D)_{amp}$, and amplitude of the lift coefficient fluctuation $(C_L)_{amp}$ of the down foil at different lateral spacings for the in-phase foil system (dashed lines represent the single foil).

lateral spacings are shown in Fig. 16(b). The dashed line represents the single foil for comparison. It is evident that the drag and lift coefficients gradually become closer to the value of the single foil with increased lateral spacing, indicating that the flow interference between the two foils is weak at large lateral spacings. Moreover, both $(C_D)_{amp}$ and $(C_L)_{amp}$ decrease with increasing lateral spacing. The results also indicate that the anti-phase foil system achieves a higher thrust production at $S = 0.3L$, while the in-phase system undergoes a drag force [as shown in Fig. 14(b)], which decreases as lateral spacing increases. This can be attributed to the strong interaction effect between the foils.

The time-averaged power coefficients C_{PW}^{ave} of each foil for the in-phase and anti-phase foil systems at varied lateral spacings are presented in Fig. 17 and the dashed line represents the single foil for comparison. Results show that C_{PW}^{ave} of both foil systems decrease with increasing lateral spacing, and the values gradually become closer to the value of the single foil at large lateral spacing. In addition, the power consumption of the anti-phase foil system is much higher than that of the in-phase foil when the foils are close due to the distinct wake dynamics and fluid force differences. The detailed vortex structure and flow feature are analyzed below to elaborate on the mechanism of thrust improvement.
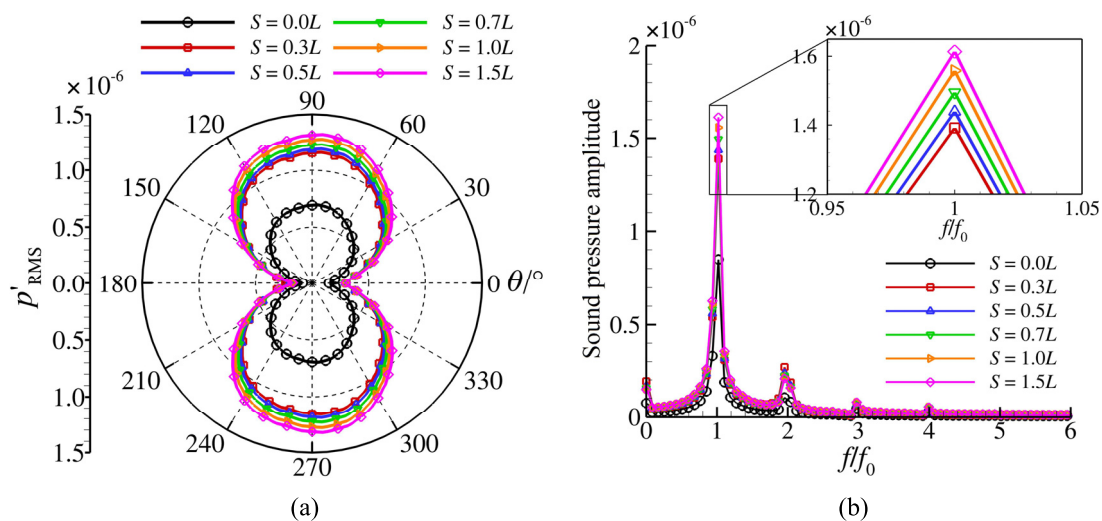

FIG. 15. Directivities (a) and frequency spectra of the sound pressure at $(60L, 90°)$ point and (b) at varied lateral spacings for the in-phase foil system.
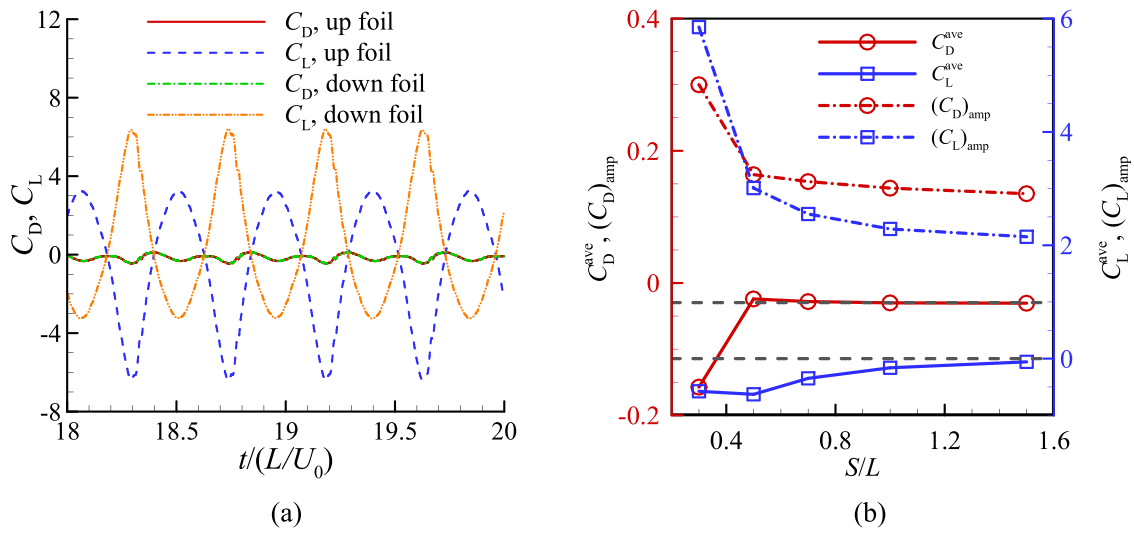
FIG. 16. (a) Time histories of drag and lift coefficients of the anti-phase foil system at $S = 0.3L$. (b) Time-averaged thrust coefficient, time-averaged lift coefficient, amplitude of the drag coefficient fluctuation, and amplitude of the lift coefficient fluctuation of down foil at varied lateral spacings for the anti-phase foil system (dashed lines represent the single foil).
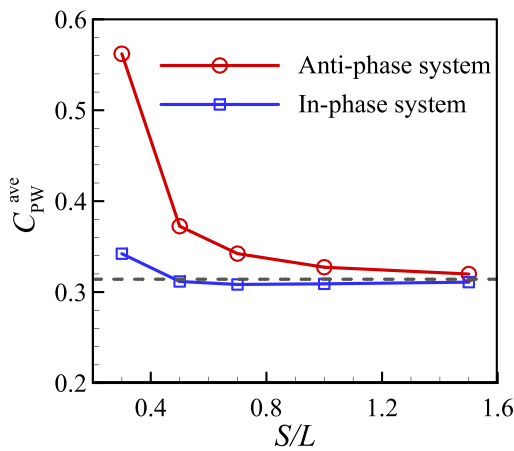

FIG. 17. Time-averaged power coefficient of each foil for the in-phase and anti-phase foil systems at varied lateral spacings (dashed line represents the single foil).

The instantaneous z-vorticity contours at lift maxima of the up and down foils at $S = 0.3L$ are presented in Fig. 18. The wake structure exhibits antisymmetric patterns about the mid-location point between the foils. As the lateral spacing between the foils is less than the width of the vortex street formed by the flow over a single foil, the flow interference between the two foils is strong, and the wake vortex presents distinct features compared with the single foil. The vortex is obviously compressed in the lateral direction due to the wall effect imposed by the neighboring foil, and vortices shed into the wake form vortex pairs rather than the vortex streets behind the foil. The time-averaged streamwise velocity contour and streamwise velocity profiles at $x/L = 100.5$, 101.0, 102.0, and 103.0 [dashed line in Fig. 19(a)] are presented in Fig. 19. A strong velocity deficit ($\overline{U}/U_0 \approx -0.5$, $y = 100.0L$) is formed in the gap region at $x/L = 100.5$ due to the formation of vortices in the gap side, as shown in Fig. 18. However, a stronger time-averaged jet is generated, which angles away from the mid-location between the foils. Therefore, the anti-phase foil system has a higher thrust production. A similar result was reported in previous studies on flow past a high-density fish school[25] and flow over a pitching airfoil near a solid boundary.[49]
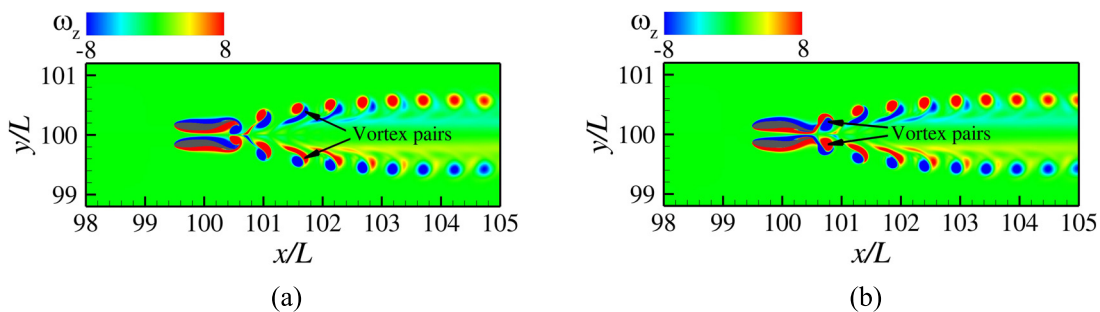

FIG. 18. Instantaneous z-vorticity contours of the anti-phase foil system at lift maxima of the up (a) and down foils (b) at $S = 0.3L$.
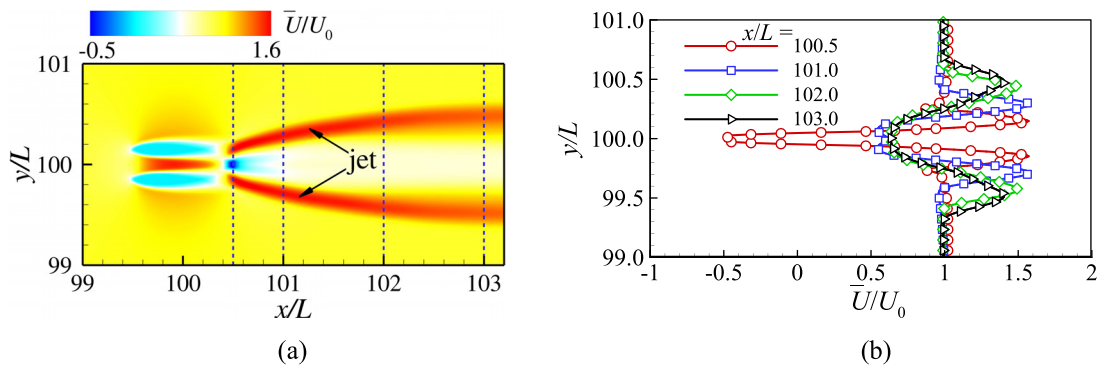
FIG. 19. Time-averaged streamwise velocity contour (a) and streamwise velocity profiles (b) at $S = 0.3L$ for the anti-phase foil system.

The instantaneous x and y components of the acoustic source distributions corresponding to Fig. 18 are shown in Fig. 20. Here, it is revealed that the acoustic source in the x direction is symmetrical with respect to the horizontal axis, while it exhibits an antisymmetric pattern in the y direction. At small lateral spacings, strong flow interference affects the acoustic source (especially in the wake vortex region), such that the distribution is obviously compressed in the lateral direction, which is consistent with the vorticity fields. The dominant acoustic sources originate mainly at the trailing and leading edges.

The instantaneous sound pressure fields of the anti-phase foil at $S = 1.5L$ in a period are presented in Fig. 21. The anti-phase foil system presents quite different features from the in-phase foil system and the single wavy foil. However, the sound pressure waves are still generated in response to vortex shedding. For the anti-phase foils, two reversed vortices are shed simultaneously from opposite sides of the foils. When a clockwise vortex is shed from the upper side of the up foil, an anticlockwise vortex is shed from the lower side of the down foil. As shown in Fig. 21(a), negative pressure is generated on the vortex-shedding sides (free-stream sides) of both foils, whereas positive pressure is generated on the gap sides. The negative sound waves generated on the free-stream sides propagate upward and downward. In this case, the sound pressure generated by the up foil is counteracted by the down foil through destructive interference, resulting in a lower sound emission in the vertical direction. Moreover, the same positive or negative sound pressure pulses are generated in the gap

region by the upper and lower foils; thus, the sound pressure in this region is amplified through constructive interference, and the amplified sound wave propagates both upstream and downstream. Therefore, the sound pressure fields generated by the anti-phase foils are always symmetrical with respect to the horizontal axis ($y = 100L$). A similar phenomenon was reported on the flow past two square cylinders in a side-by-side arrangement in the anti-phase synchronized pattern.[50] The lower sound emission in the vertical direction and the amplified sound pressure in the horizontal direction lead to a monopole-like pattern.

The instantaneous sound pressure fields of the anti-phase system at various lateral spacings are presented in Fig. 22, with the single foil ($S = 0.0L$) also shown for comparison. From the figure, it is evident that all the sound pressure fields present a monopole-like distribution. However, different features can be observed at varied lateral spacings. The strong and weak waves generate alternately, and the amplitude of the strong sound wave gradually approaches the value of the weak sound wave with increasing lateral spacing, especially at the large lateral spacing in Fig. 22(f). It is also revealed that the differences decrease gradually with increased lateral spacing, as the flow interference between the two foils is weak. For example, the sound pressure field at $S = 1.0L$ in Fig. 22(e) is very similar to that of $S = 1.5L$ in Fig. 22(f).

The frequency spectra of sound pressure measured at $r = 60L$, $\theta = 0°$, $90°$, $180°$, and $270°$ at varied lateral spacings for the anti-phase foil system are presented in Fig. 23. It is obvious that the undulatory
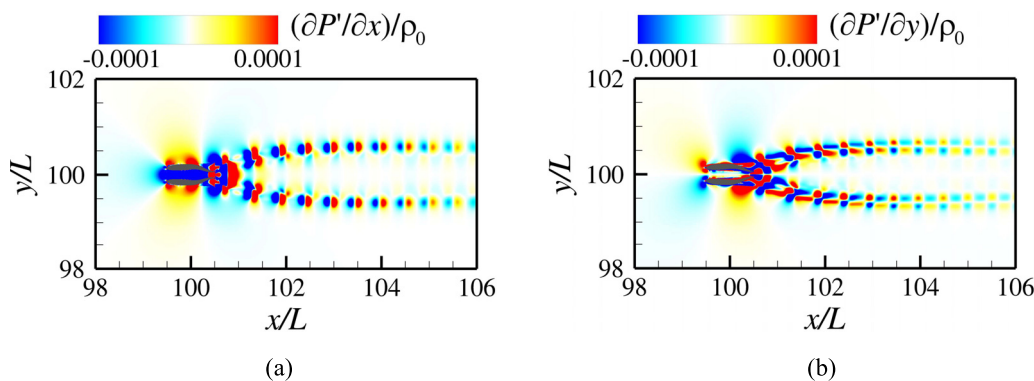

FIG. 20. Instantaneous acoustic source distributions of x component (a) and y component (b) for the anti-phase foil system at $S = 0.3L$.
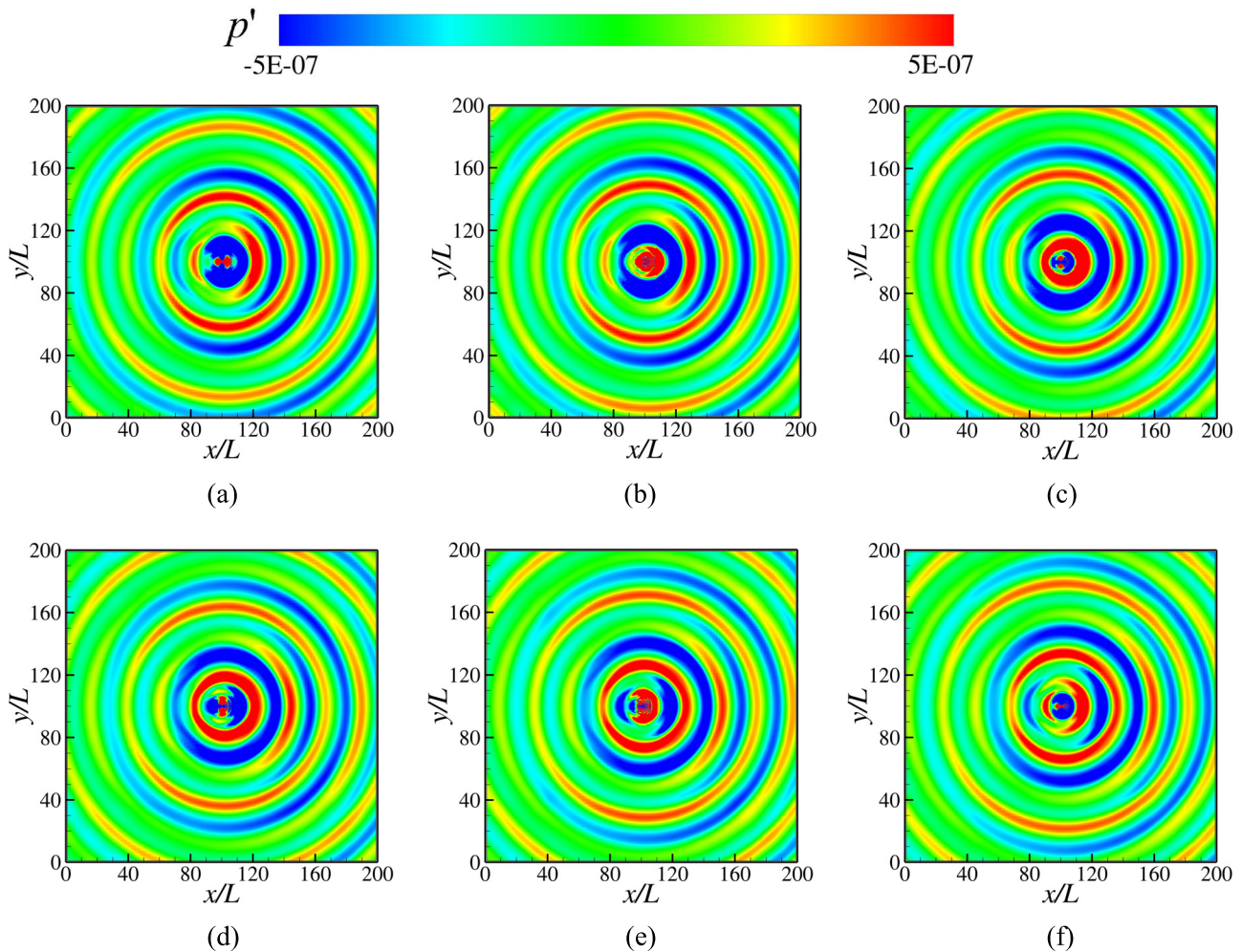
FIG. 21. Instantaneous sound pressure fields of the anti-phase foil system at $S = 1.5L$ in a period. (a) $t = 0/6T$, (b) $t = 1/6T$, (c) $t = 2/6T$, (d) $t = 3/6T$, (e) $t = 4/6T$, and (f) $t = 5/6T$.

frequency f_0 and its first even harmonics at $2f_0$ play the strongest role in sound emission. Although third- and fourth-order harmonics are also observed, the contributions at these frequencies decrease significantly. Different from the single foil, where the sound pressure at a frequency of f_0 is significantly higher than at a frequency of $2f_0$, the sound generated by anti-phase foils at a frequency of $2f_0$ is comparable to that of f_0, and both harmonics dominate all directions when $S \leq 0.7L$. With increased lateral spacing, the amplitudes of f_0 gradually decrease in the horizontal direction ($0°$ and $180°$), and the sound contributions are very small at $S = 1.0L$ and $1.5L$.

The sound directivities measured at a distance of $r = 60L$ at varied lateral spacings are shown in Fig. 24(a), and the single foil ($S = 0.0L$) is also plotted for comparison. Here, it is clear that the sound pressure generated by the anti-phase foil system is smaller than the single foil in the vertical direction, especially when $S \geq 0.5L$. All the directivities of the anti-phase foils present a monopole-like pattern, and the amplitudes in all directions decrease monotonically with increasing lateral spacing. The sound pressure is maximum at $S = 0.3L$

in the anti-phase system, indicating that the flow interference between the foils could improve the thrust, while simultaneously generating higher radiation of sound. By compared with the in-phase foil system in Fig. 15(a), it is revealed that the magnitudes of the sound pressures of the anti-phase cases are lower than the in-phase cases, which are approximately twice the amplitude of the single foil. The difference between foil systems in the sound pressure field can be attributed to the different wake patterns and flow performance, which is originally controlled by varied kinematics, including phase difference and lateral spacing.

The effective sound pressure in four directions against lateral spacing is presented in Fig. 24(b), where it is evident that the maximum sound pressure appears in the downstream direction ($0°$). The amplitudes at $90°$ and $270°$ are the same, and $180°$ is the minimum. The amplitudes of sound pressure in the four directions decrease with increasing lateral spacing, and the maximum sound pressure almost reduces by 50% at $S = 0.5L$ (4.1×10^{-7}) compared with that of $S = 0.3L$ (7.6×10^{-7}). However, the directivities at $S \geq 0.7L$ do not
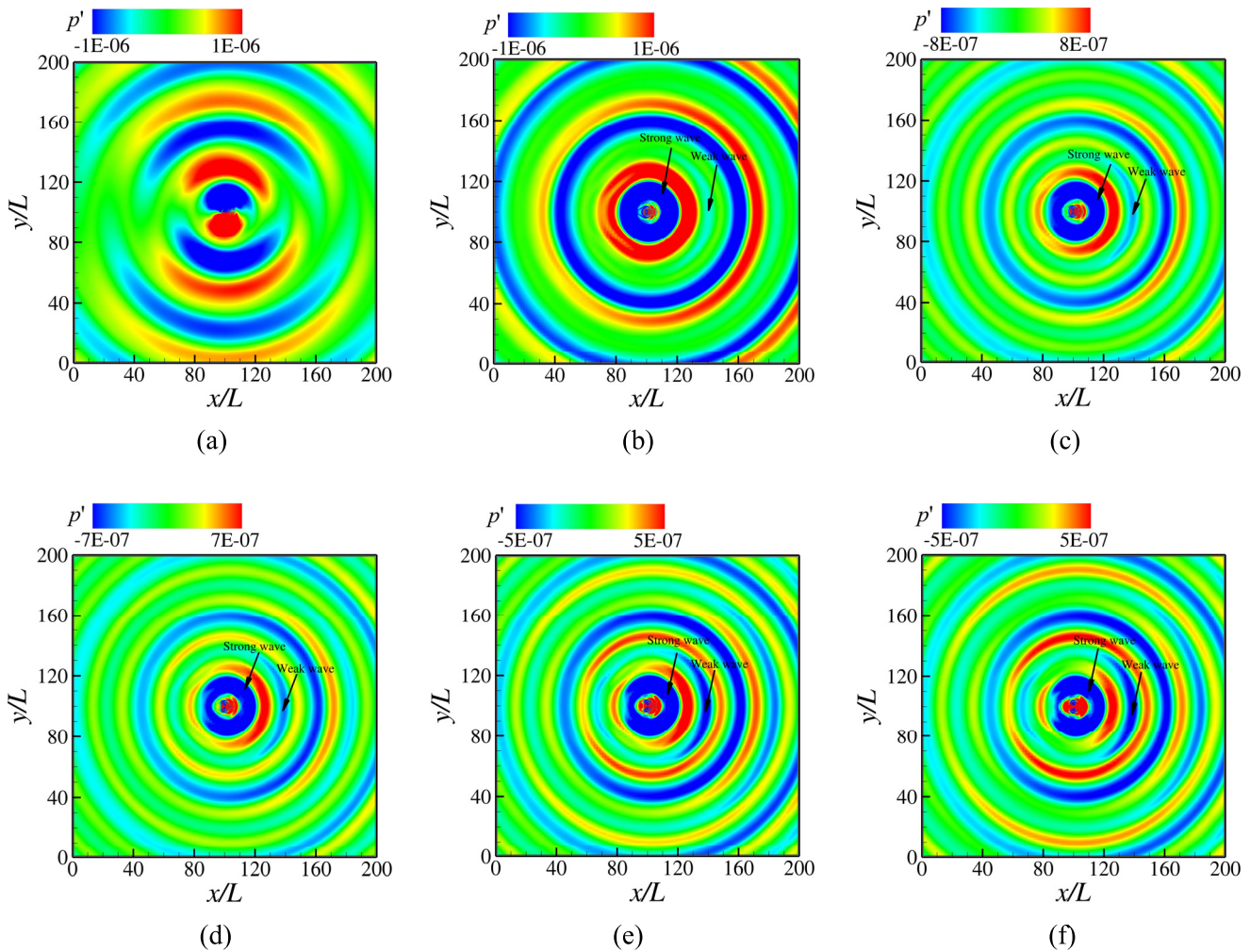
FIG. 22. Instantaneous sound pressure fields at varied lateral spacing for the anti-phase foil system. (a) $S = 0.0L$, (b) $S = 0.3L$, (c) $S = 0.5L$, (d) $S = 0.7L$, (e) $S = 1.0L$, and (f) $S = 1.5L$.

change significantly. In particular, it should be noted that $S = 1.0L$ generates a pattern that is very close to that of $S = 1.5L$, as flow interference plays a very weak role in the sound pressure field. The effect of lateral spacing on sound pressure can be explained by the fluid force coefficients, including variations in both the lift and thrust coefficients. The effective sound pressure against lateral spacing in Fig. 24(b) presents a pattern similar to that in Fig. 16(b), in which both $(C_T)_{amp}$ and $(C_L)_{amp}$ decrease with increasing lateral spacing, resulting in a decrease in sound pressure.

The frequency spectrum analysis indicated that the sound pressure field of the anti-phase foil system is dominated by the first harmonic f_0 and second harmonic $2f_0$, and a more robust comparison that considers the acoustic directivities at varied lateral spacings is shown in Fig. 25. This reveals that f_0 transforms from a monopole-like sound source to a dipole-like sound source with increasing lateral spacing, with a dipole clearly observable at $S = 1.5L$ in Fig. 25(f). However, a monopole-like radiation pattern is presented at the second

harmonic for all lateral spacings. Moreover, the magnitudes of both sound pressures at f_0 and $2f_0$ decrease gradually with increased lateral spacing and remain a minor change when $S \geq 0.7L$.

Previous studies have indicated that the directivities of the sound pressure are closely related to the fluid force coefficients.[17,19,21] For the single foil, the frequency of the drag coefficient is twice that of the lift coefficient, and the first harmonic f_0 presents a lift dipole. For the anti-phase foil system, the frequency of the lift coefficient is equal to the drag coefficient at small lateral spacings [as shown in Fig. 16(a)], and both force coefficients are dominated by the first harmonic, f_0; hence, a monopole-like radiation pattern is presented. Both $(C_T)_{amp}$ and $(C_L)_{amp}$ decrease with increasing lateral spacing, resulting in a decrease in sound pressure at f_0 and $2f_0$. When the lateral spacing is large, the flow interference between the foils is very weak and a lift dipole is presented, which is similar to the single foil. When compared with the single foil, it is found that the sound pressure at $2f_0$ is twice the amplitude of the single foil, which is in agreement with the flow results
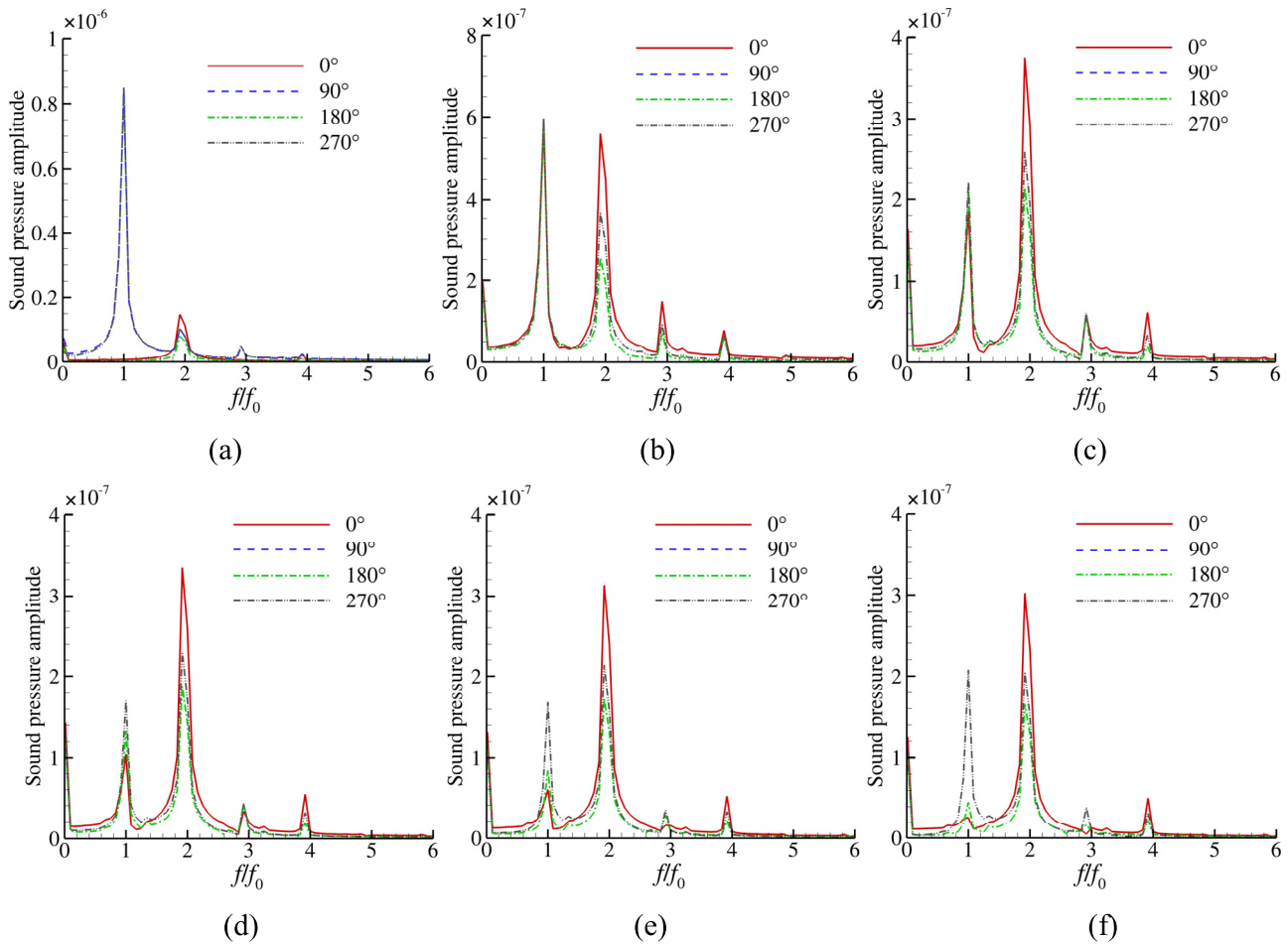
FIG. 23. Frequency spectra of sound pressure measured at $r = 60L$, $\theta = 0°$, $90°$, $180°$, and $270°$ at varied lateral spacings for the anti-phase foil system. (a) $S = 0.0L$, (b) $S = 0.3L$, (c) $S = 0.5L$, (d) $S = 0.7L$, (e) $S = 1.0L$, and (f) $S = 1.5L$.

shown in Fig. 16(a), where the drag coefficients of the anti-phase foils are in phase.

IV. CONCLUSIONS

In this study, the sound generated by flow over two traveling wavy foils in a side-by-side arrangement at a Reynolds number of 1000 is investigated using a hybrid method based on the immersed boundary method. The hydrodynamics and sound pressure field for the flow over in-phase and anti-phase foils are analyzed. The results indicate that the phase difference and flow interference between the foils have a significant influence on the flow performance and the sound pressure field. The main results are summarized as follows.

The sound generated by flow over a single foil is dipole-like, and the lift dipole seems to dominate the sound pressure field. The threshold St values of thrust generation for the LA–HF and HA–LF foils are 0.42 and 0.57, respectively. When St is constant, the LA–HF foil achieves higher thrust by increasing the power consumption compared with the HA–LF foil. Moreover, the magnitude of the sound pressure radiated from the LA–HF foil is greater than that of the HA–LF foil due to the larger amplitude of the lift fluctuation.

In terms of the foil system with $St = 0.45$, the flow structure and sound pressure field present distinct features depending on the phase difference. In the in-phase case, two vortex streets are shed synchronously and merge into one when the foils are close. However, the vortices of the anti-phase case shed into the wake to form pairs, and angled jets of mean momentum are generated, resulting in higher thrust production. For the sound pressure field, the in-phase foil system presents a dipole-like pattern, whereas the anti-phase foil system presents a monopole-like pattern. In addition, the lateral spacing between the two foils has a different effect on the magnitude of the sound pressure, which increases slightly with increasing lateral spacing in the in-phase case. However, the sound pressure decreases rapidly when $S < 0.7L$ and then remains nearly unchanged when $S > 0.7L$ in the anti-phase case. This can be attributed to the amplitudes of fluid force fluctuations, including the lift and drag fluctuations. A comparison of the two kinds of foil systems implies that the power consumption of the anti-phase system is higher, and the thrust is significantly improved compared with the in-phase system due to the distinct difference in wake patterns. However, the magnitude of the sound
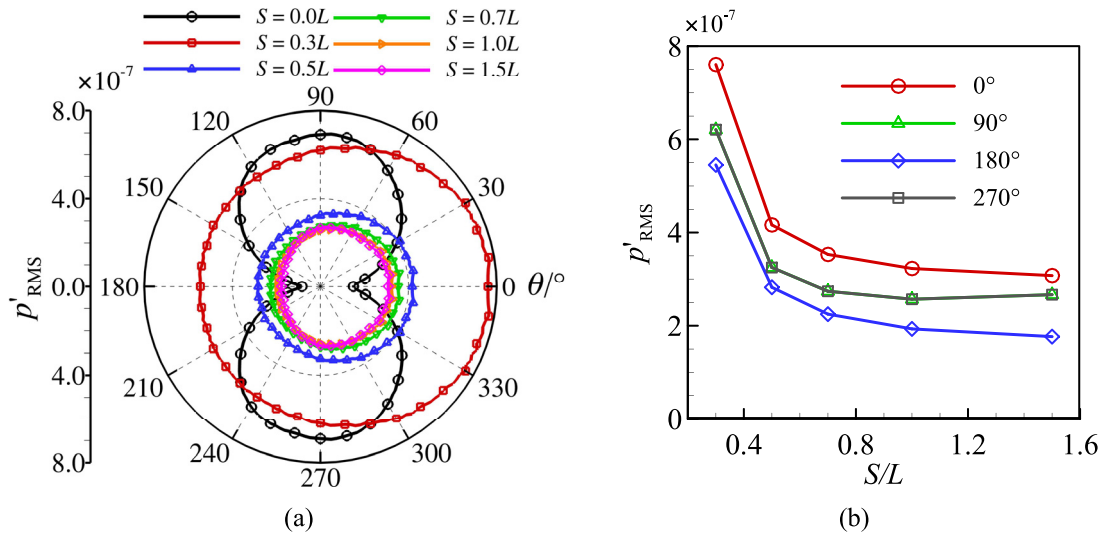
FIG. 24. (a) Sound directivities of the anti-phase foil system at varied lateral spacings. (b) Effective sound pressure in four directions against the lateral spacing for the anti-phase foil system.
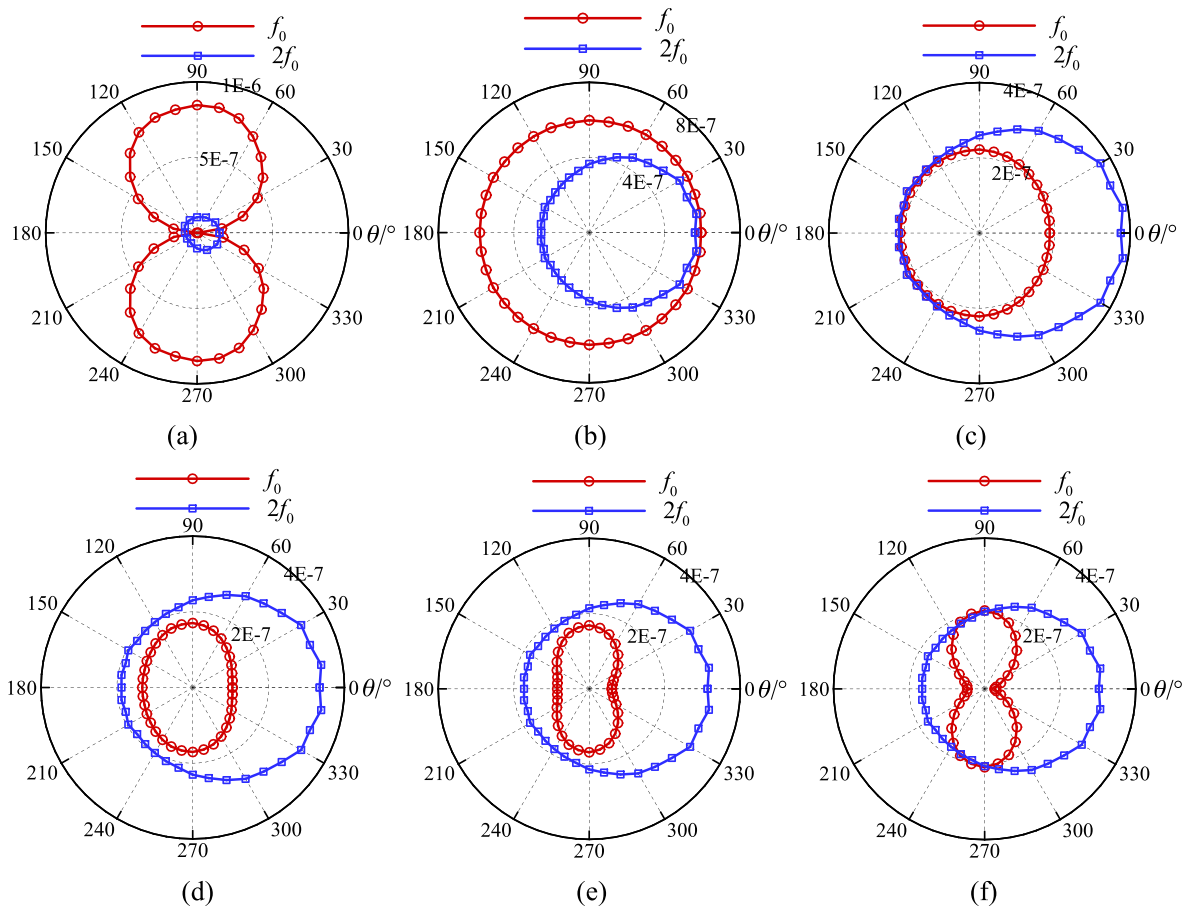

FIG. 25. Polar diagrams of sound pressure amplitude of the first harmonic and the second harmonic at varied lateral spacings for the anti-phase foil system. (a) $S = 0.0L$, (b) $S = 0.3L$, (c) $S = 0.5L$, (d) $S = 0.7L$, (e) $S = 1.0L$, and (f) $S = 1.5L$.

pressure generated by the anti-phase foil system is lower than that generated by the in-phase system.

The presented results would be helpful for understanding the hydrodynamics and corresponding sound pressure field of a navigator with multiple undulating foils, and elucidate the sound generation of fish schooling and collective swimming of man-made underwater vehicles. Although only two typical cases (in-phase and anti-phase motions) are considered in this paper, more phase differences and other configurations (such as two or more foils in tandem) might be desirable in future work.

ACKNOWLEDGMENTS

AUTHOR DECLARATIONS
Conflict of Interest

The authors have no conflicts to disclose.

Author Contributions

Cheng Zhao: Formal analysis (equal); Methodology (equal); Validation (equal); Writing – original draft (equal). **Tao Zhang:** Conceptualization (equal); Funding acquisition (equal); Supervision (equal); Writing – review & editing (equal). **Yan Yang:** Funding acquisition (equal); Methodology (equal); Software (equal); Writing – review & editing (equal). **Haibo Dong:** Software (equal); Writing – review & editing (equal).

DATA AVAILABILITY

The data that support the findings of this study are available from the corresponding author upon reasonable request.

NOMENCLATURE

a_{max}	tail beat amplitude
C_D, C_T, C_L	drag coefficient, thrust coefficient, and lift coefficient
$(C_D)_{amp}$	amplitude of the drag coefficient fluctuation
$(C_L)_{amp}$	amplitude of the lift coefficient fluctuation
c_0	speed of sound
C_D^{ave}, C_L^{ave}	time-averaged drag coefficient and time-averaged lift coefficient
C_L^{RMS}	RMS value of the lift coefficient
C_{PW}	power coefficient
D	diameter of the cylinder
F_D, F_L, P_f	drag, lift, and power
f_0	undulatory frequency
k	wave number
L	chord length of the foil
Ma	Mach number
P'	incompressible perturbation pressure
p'	sound pressure
p'_{RMS}	effective sound pressure
r	radius of the sound directivity
R^2	coefficient of determination
Re	Reynolds number
S	lateral spacing between the foils
St	Strouhal number
$\boldsymbol{u'}$	perturbation velocity
U_0	incoming flow velocity
θ	angle of the sound directivity
ρ_0	density of the fluid
v_0	kinematic viscosity of the fluid
φ	initial phase angle
ω_z	z-vorticity

REFERENCES

[1]T. Y. Wu, "Fish swimming and bird/insect flight," Annu. Rev. Fluid Mech. **43**, 25 (2011).

[2]G. V. Lauder, "Fish locomotion: Recent advances and new directions," Annu. Rev. Mar. Sci. **7**, 521 (2015).

[3]J. H. Costello, S. P. Colin, J. O. Dabiri, B. J. Gemmell, K. N. Lucas, and K. R. Sutherland, "The hydrodynamics of jellyfish swimming," Annu. Rev. Mar. Sci. **13**, 375 (2021).

[4]G. Liu, Y. Ren, H. Dong, O. Akanyeti, J. C. Liao, and G. V. Lauder, "Computational analysis of vortex dynamics and performance enhancement due to body–fin and fin–fin interactions in fish-like locomotion," J. Fluid Mech. **829**, 65 (2017).

[5]Y.-L. Yu and K.-J. Huang, "Scaling law of fish undulatory propulsion," Phys. Fluids **33**, 061905 (2021).

[6]C. Guo, Y. Kuai, Y. Han, P. Xu, Y. Fan, and C. Yu, "Hydrodynamic analysis of propulsion process of zebrafish," Phys. Fluids **34**, 021910 (2022).

[7]P. Choudhary and S. B. Babu, "Increasing the efficiency and maneuverability of one-hinge swimmer," Phys. Fluids **33**, 071901 (2021).

[8]Y. Luo, T. Xu, Q. Huang, Z. Hou, and G. Pan, "A numerical investigation on thrust and torque production of a batoid fish with asymmetric pectoral fins flapping," Ocean Eng. **263**, 112342 (2022).

[9]C. Wei, Q. Hu, Y. Liu, S. Yin, Z. Chen, and X. Ji, "Performance evaluation and optimization for two-dimensional fish-like propulsion," Ocean Eng. **233**, 109191 (2021).

[10]G. J. Dong and X. Y. Lu, "Characteristics of flow over traveling wavy foils in a side-by-side arrangement," Phys. Fluids **19**, 057107 (2007).

[11]Q. Zhong, J. Zhu, F. E. Fish, S. J. Kerr, A. M. Downs, H. Bart-Smith, and D. B. Quinn, "Tunable stiffness enables fast and efficient swimming in fish-like robots," Sci. Robot. **6**, eabe4088 (2021).

[12]J. Sueur, E. J. Tuck, and D. Robert, "Sound radiation around a flying fly," J. Acoust. Soc. Am. **118**, 530 (2005).

[13]L. J. Cator, B. J. Arthur, L. C. Harrington, and R. R. Hoy, "Harmonic convergence in the love songs of the dengue vector mosquito," Science **323**, 1077 (2009).

[14]J.-H. Seo, T. L. Hedrick, and R. Mittal, "Mechanism and scaling of wing tone generation in mosquitoes," Bioinspiration Biomimetics **15**, 016008 (2019).

[15]J.-H. Seo, T. L. Hedrick, and R. Mittal, "Mosquitoes buzz and fruit flies don't-a comparative aeroacoustic analysis of wing-tone generation," Bioinspiration Biomimetics **16**, 046019 (2021).

[16]Y. Bae and Y. J. Moon, "Aerodynamic sound generation of flapping wing," J. Acoust. Soc. Am. **124**, 72 (2008).

[17]B. Geng, Q. Xue, X. Zheng, G. Liu, Y. Ren, and H. Dong, "The effect of wing flexibility on sound generation of flapping wings," Bioinspiration Biomimetics **13**, 016010 (2017).

[18]K. Nedunchezian, C-k Kang, and H. Aono, "Effects of flapping wing kinematics on the aeroacoustics of hovering flight," J. Sound Vib. **442**, 366 (2019).

[19]L. Wang and F.-B. Tian, "Numerical study of flexible flapping wings with an immersed boundary method: Fluid–structure–acoustics interaction," J. Fluid Struct. **90**, 396 (2019).

[20]L. Wang and F.-B. Tian, "Numerical study of sound generation by three-dimensional flexible flapping wings during hovering flight," J. Fluid Struct. **99**, 103165 (2020).

[21]M. S. U. Khalid, I. Akhtar, and B. Wu, "Quantification of flow noise produced by an oscillating hydrofoil," Ocean Eng. **171**, 377 (2019).

[22]N. Wagenhoffer, K. W. Moored, and J. W. Jaworski, "Unsteady propulsion and the acoustic signature of undulatory swimmers in and out of ground effect," Phys. Rev. Fluids **6**, 033101 (2021).

[23]Y. Bao, D. Zhou, J. J. Tao, Z. Peng, H. B. Zhu, Z. L. Sun, and H. L. Tong, "Dynamic interference of two anti-phase flapping foils in side-by-side arrangement in an incompressible flow," Phys. Fluids **29**, 033601 (2017).

[24]M. Kurt, A. E. Panah, and K. W. Moored, "Flow interactions between low aspect ratio hydrofoils in in-line and staggered arrangements," Biomimetics **5**, 13 (2020).

[25]Y. Pan and H. Dong, "Computational analysis of hydrodynamic interactions in a high-density fish school," Phys. Fluids **32**, 121901 (2020).

[26]A. Gilmanov and F. Sotiropoulos, "A hybrid Cartesian/immersed boundary method for simulating flows with 3D, geometrically complex, moving bodies," J. Comput. Phys. **207**, 457 (2005).

[27]J. J. Videler and F. Hess, "Fast continuous swimming of two pelagic predators, saithe (*Pollachius Virens*) and mackerel (*Scomber Scombrus*): A kinematic analysis," J. Exp. Biol. **109**, 209 (1984).

[28]H. Liu and K. Kawachi, "A numerical study of undulatory swimming," J. Comput. Phys. **155**, 223 (1999).

[29]Y. Sui, Y. T. Chew, P. Roy, and H. T. Low, "A hybrid immersed-boundary and multi-block lattice Boltzmann method for simulating fluid and moving-boundaries interactions," Int. J. Numer. Meth. Fluids **53**, 1727 (2007).

[30]H. Liu, R. Wassersug, and K. Kawachi, "A computational fluid dynamics study of tadpole swimming," J. Exp. Biol. **199**, 1245 (1996).

[31]M. S. U. Khalid, I. Akhtar, and H. Dong, "Hydrodynamics of a tandem fish school with asynchronous undulation of individuals," J. Fluid Struct. **66**, 19 (2016).

[32]H. Liu, R. Wassersug, and K. Kawachi, "The three-dimensional hydrodynamics of tadpole locomotion," J. Exp. Biol. **200**, 2807 (1997).

[33]C. K. Hemelrijk, D. A. P. Reid, H. Hildenbrandt, and J. T. Padding, "The increased efficiency of fish swimming in a school," Fish Fish. **16**, 511 (2015).

[34]H. Dong, R. Mittal, and F. M. Najjar, "Wake topology and hydrodynamic performance of low-aspect-ratio flapping foils," J. Fluid Mech. **566**, 309 (2006).

[35]R. Mittal, H. Dong, M. Bozkurttas, F. M. Najjar, A. Vargas, and A. Von Loebbecke, "A versatile sharp interface immersed boundary method for incompressible flows with complex boundaries," J. Comput. Phys. **227**, 4825 (2008).

[36]P. Han, G. V. Lauder, and H. Dong, "Hydrodynamics of median-fin interactions in fish-like locomotion: Effects of fin shape and movement," Phys. Fluids **32**, 011902 (2020).

[37]M. S. U. Khalid, J. Wang, I. Akhtar, H. Dong, M. Liu, and A. Hemmati, "Larger wavelengths suit hydrodynamics of carangiform swimmers," Phys. Rev. Fluids **6**, 073101 (2021).

[38]Y. Pan and H. Dong, "Effects of phase difference on hydrodynamic interactions and wake patterns in high-density fish schools," Phys. Fluids **34**, 111902 (2022).

[39]R. Ewert and W. Schröder, "Acoustic perturbation equations based on flow decomposition via source filtering," J. Comput. Phys. **188**, 365 (2003).

[40]C. K. W. Tam and J. C. Webb, "Dispersion-relation-preserving finite difference schemes for computational acoustics," J. Comput. Phys. **107**, 262 (1993).

[41]F. Q. AerospaceJournal of experimental biologyHu, M. Y. Hussaini, and J. L. Manthey, "Low-dissipation and low-dispersion Runge–Kutta schemes for computational acoustics," J. Comput. Phys **124**, 177 (1996).

[42]C. Bogey and C. Bailly, "A family of low dispersive and low dissipative explicit schemes for flow and noise computations," J. Comput. Phys **194**, 194–214 (2004).

[43]C. K. W. Tam and Z. Dong, "Radiation and outflow boundary conditions for direct computation of acoustic and flow disturbances in a nonuniform mean flow," J. Comput. Acoust. **4**, 175 (1996).

[44]C. Zhao, Y. Yang, T. Zhang, and H. Dong, "Numerical simulation of acoustic scattering and flow-induced noise with sharp interface immersed boundary method," AIAA Paper No. 2020-0336.

[45]C. Zhao, Y. Yang, T. Zhang, H. Dong, and G. Hou, "A sharp interface immersed boundary method for flow-induced noise prediction using acoustic perturbation equations," Comput. Fluids **227**, 105032 (2021).

[46]C. Zhao, T. Zhang, and G. Hou, "Finite-difference time-domain modeling for underwater acoustic scattering applications based on immersed boundary method," Appl. Acoust. **193**, 108764 (2022).

[47]Y. Hattori and R. Komatsu, "Mechanism of aeroacoustic sound generation and reduction in a flow past oscillating and fixed cylinders," J. Fluid Mech. **832**, 241 (2017).

[48]O. Inoue and N. Hatakeyama, "Sound generation by a two-dimensional circular cylinder in a uniform flow," J. Fluid Mech. **471**, 285 (2002).

[49]D. B. Quinn, K. W. Moored, P. A. Dewey, and A. J. Smits, "Unsteady propulsion near a solid boundary," J. Fluid Mech. **742**, 152 (2014).

[50]O. Inoue, W. Iwakami, and N. Hatakeyama, "Aeolian tones radiated from flow past two square cylinders in a side-by-side arrangement," Phys. Fluids **18**, 046104 (2006).